# Control of 3D Human Arm Impedance

by

Harshil Naresh Patel

A Thesis Presented in Partial Fulfillment
of the Requirements for the Degree
Master of Science

Approved April 2013 by the
Graduate Supervisory Committee:

Panagiotis Artemiadis, Chair
Spring Berman
Stephen Helms Tillery

ARIZONA STATE UNIVERSITY

May 2013

ABSTRACT

Humans have an inherent capability of performing highly dexterous and skillful tasks with their arms, involving maintaining posture, movement and interacting with the environment. The latter requires for them to control the dynamic characteristics of the upper limb musculoskeletal system. Inertia, damping and stiffness, a measure of mechanical impedance, gives a strong representation of these characteristics. Many previous studies have shown that the arm posture is a dominant factor for determining the end point impedance in a horizontal plane (transverse plane). The objective of this thesis is to characterize end point impedance of the human arm in the three dimensional (3D) space. Moreover, it investigates and models the control of the arm impedance due to increasing levels of muscle co-contraction. The characterization is done through experimental trials where human subjects maintained arm posture, while perturbed by a robot arm. Moreover, the subjects were asked to control the level of their arm muscles' co-contraction, using visual feedback of their muscles' activation, in order to investigate the effect of the muscle co-contraction on the arm impedance. The results of this study showed a very interesting, anisotropic increase of the arm stiffness due to muscle co-contraction. This can lead to very useful conclusions about the arm biomechanics as well as many implications for human motor control and more specifically the control of arm impedance through muscle co-contraction. The study finds implications for the EMG-based control of robots that physically interact with humans.

ACKNOWLEDGEMENTS

I would like to express my sincere gratitude to my advisor, Dr. Artemiadis, for the continuous support throughout my Master's program, for his patience, motivation, enthusiasm, immense knowledge and the opportunity to work with the KUKA arm. I thank my fellow lab mates in the HORC lab for stimulating discussions and for all the fun we have had in the last two years. Last but not the least, I would like to thank my late grandmother and my parents for their blessings and my sisters for their love. And although this may seem unfair, a special thanks to my older sister Kinnari.

TABLE OF CONTENTS

LIST OF TABLES

LIST OF FIGURES

# Chapter 1

# INTRODUCTION

Skeletal muscles are actuators which drive natural limb movements in living beings. Research on human motor control has led to a wide range of opinions concerning the strategy of the central nervous system (CNS) in controlling these limb movements. Researchers have suggested control of muscle variables such as length, force, velocity, stiffness and damping. The difficulty in postulating a single strategy, considering the vast complexity of the CNS and a great variety of task of which it is capable of, has been recognized in [35] . Since the late 70's it has been made clear that it is not adequate to regard muscles simply as a generator of force. Inertia, damping and stiffness, three basic components of mechanical impedance that relate force to acceleration, velocity and position respectively in both static and dynamic cases, have been shown to play an important role in control of posture along with movement [6], [4], [3], [16], [17] and [20]. Such an approach is based on the understanding that the complex functionality of the CNS has been developed by the need not only to control tasks, but also to take advantage of the mechanical properties of the musculo-skeletal system [5]. This approach was introduced in [12] that investigated the spring-like properties of the human arm. Muscles do indeed behave like tune-able springs in the sense that the force generated by them is a function of the length and level of neural activation. The muscles are arranged about the joints in a fashion such that an equal but opposite force generated in these agonist and antagonist muscles sub-serve posture maintenance in the limb. This implies that when a force from the environment is applied, the limb is displaced by an amount proportional to both the external force and the stiffness of the muscles. And due to the spring-like property, the limb should return to the the initial position when the force is removed. This prediction is analogous to the Hook's law in a bio-mechanical context.

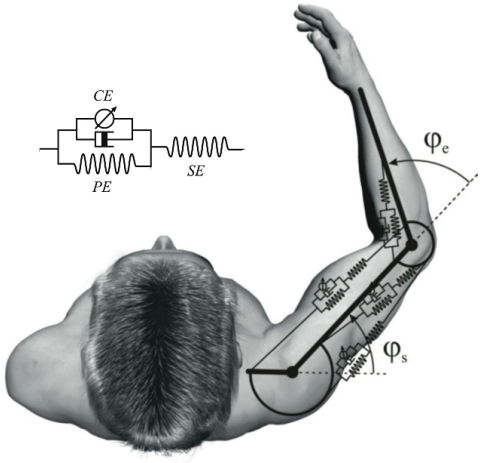


Figure 1.1: From [21] : Schematic of a musculoskeletal model of the upper limb and Hill-type muscle unit. CE, contractile element; PE, parallel elastic element; SE, series elastic element

Other studies [33], [19] and [20] postulate a motor control mechanism underlying human limb movement, consisting of a mass-spring-damper system. Their observations led to a control hypothesis according to which the CNS controls movement by specifying the final equilibrium point and details of the trajectory to follow. These factors are determined from the inherent inertial and viscoelastic properties of the limb and muscles. In [5] it was also concluded that the position of the limb, at which the length-dependent forces due to opposing agonist and antagonist muscles are equal, is an equilibrium position. Movement is thus a transition from one arm posture to another achieved by adjusting the relative control of the lenght and neural activation to each of these opposing muscles so that the equilibrium point defined by their interaction is moved towards the target position.

Given the importance of mechanical impedance, many studies show that the CNS can modulate the mechanical impedance [18], [24], [23] and [28]. Manipulation of objects in the environment requires mechanical interaction with it. For successful interaction with the object, the CNS chooses the mechanical impedance to control the behavior of the complete system, the hand and the environment. Theories and experiments regarding human limb impedance control have progressed historically from consideration of single

muscles to the investigation of the multi-joint limbs. Several experiments [26], [38], [32] have been conducted to characterize human arm endpoint stiffness using different methods. All of these experimental measurements concentrated on measuring the static component of impedance i.e., stiffness, in posture maintenance scenarios in a horizontal (transverse) plane. Dolan et. al. [11] extended it to the measurement of damping and inertia, the other two components of mechanical impedance, again in 2D space. This thesis presents a method of characterizing the human arm mechanical impedance for posture maintenane in 3D space and how the CNS controls the mechanical impedance through muscle co-contraction.

## 1.1 Motivation

Among the various interactions of the human upper limbs with the environment, a wide range of applications involving physical interaction of robots with humans has received increased attention in the last few decades. Most of the tasks that humans perform where they are interacting with the environment are performed in a 3D workspace. These include tasks like working with tools to cut, drill, build, etc. Lifting masses from the floor to place them at a height, moving masses from left to right and vice versa or moving with masses held in our arms. And even day-to-day tasks like opening windows, washing utensils etc., all are performed in a 3D workspace. The interest of the study presented in this thesis is directed towards developing EMG based robotic prosthetic and orthotic devices. In the case of a prosthetic devices, the rationale is to design a prosthetic device that can mimic an actual arm making it's use life-like for the amputees. In case of the orthotic devices (exoskeletons), the rationale is to design a device that interacts with the natural dynamics of the arm for different modes of operation. These different modes could be of rehabilitative, assistive or augmentative in nature. Rehabilitation robotics makes the use of robot arms to rehabilitate patients who have lost all or partial control of their own limbs. The rehabilitation robots are essentially designed to impart a more effective therapy compared to the physical therapist. Assistive robots like the PR2 [8] have been developed to enable people

with severe motor impairments, to interact with their own bodies and their environments, thereby improving their quality of life. Augmentative robot arms find applications in the military and manufacturing industry. All of this calls for pre-developmental characterization of the mechanical impedance of the human limbs which can then be incorporated in the controllers for all these robotic devices.

## 1.2 Objective

In this thesis, a systematic method for characterizing human arm end point impedance in the 3D space and how it is controlled through muscle co-contraction is presented. The rationale of the study is to extend the previous methods of characterizing the human arm end point impedance from a 2D space (horizontal plane) to a 3D space and more importantly, how humans can control it through co-contracting muscles of the arm. Ellipsoids are used to represent all the components (inertia, damping and stiffness) 3D end point impedance. This gives us a precise representation of the magnitude, proportion and directionality of these components through the size, shape and orientation of the ellipsoids. Ellipsoids for various human arm configurations at various co-contraction levels are then compared to form a basis for studying how the human arm end point impedance is controlled.

## 1.3 Overview

Chapter 2 explores the previous studies done in the field. The beginning section reviews the experimental setups and the methods previously employed to identify impedance, mainly stiffness, in a horizontal (transverse) plane. The next section introduces techniques used to estimate the impedance and methods to represent it followed by the few studies initiated towards studying how impedance is modulated. Chapter 3 introduces the proposed method for the impedance characterization in 3D space. It provides a thorough explanation of all stages of the experimentation designed for the study. Chapter 4 presents the data analysis framework applied to the database of forces and displacements collected from the experiments to characterize the impedance components. It provides an explanation of the proposed impedance representation methods as well as a discussion of the results. Finally,

Chapter 6 summarizes the findings of the thesis and adds insight into continuing and future work.

# Chapter 2

# BACKGROUND LITERATURE

As explained in the previous section the need to characterize the human arm impedance, whether it is the joint impedance or the the end point, has been recognized since the early 80's. Since then many methods have been introduced to measure the impedance. All these methods have been employed to characterize the impedance in a 2D space. Most of the interactions done by human in the application explained in section 1.1 with the environment are in a 3D space. Very few have followed to characterization of human arm impedance in a 3D space. Since the method proposed in this thesis is based off from the evolving methods that characterize human arm impedance in 2D space, it is important to review all these methods. Accordingly, this chapter begins with the methods employed previously. Few researchers have investigated how the impedance is modulated through muscle activation, again in 2D space, which is discussed in the section that follows. The last section helps give context to the rationale of this thesis.

## 2.1 Introduction

Mussa-Ivaldi et. al. [26] reported a study that was directed at understanding the process subserving posture stability of the upper arm, explained in chapter 1. The goal in their investigation was to develop a method to characterize the spring-like behavior of all the muscles in the arm. To deal with the richer and more complex situation in a multi-joint arm, they developed a new approach to study posture and movement. This approach entailed displacing the hand in many different direction and each time determining the restoring forces. This restoring force consisted of a static component that was related to both magnitude and direction of the displacement from the equilibrium position through stiffness given by Hooke's Law. The stiffness was estimated by using standard linear regression procedure. They developed a compact and mathematically concise representation of representing the stiffness using ellipses. This method formed the basis for other methods

proposed thereafter as discussed below. The schemes of determining stiffness can be divided into two based on the method of displacing the arm. Some studies have employed random stochastic perturbation of short duration, while some methods have employed force regulation tasks, where the subjects are instructed to produce a specific magnitude of force while moving in a particular direction. Both methods assume a linear relationship between force and displacement.

## 2.2 Experimental Setup and Apparatus

In the experimental setup in [26], [11], [7], [38], [36] and [30] subjects were seated with the shoulder restrained to the chair by a shoulder harness belt, and the right hand gripped the handle of a two-link manipulandum as shown in Fig.2.1. The wrist and the palm were either bandaged with a gauze, which was also wrapped around the handle of the manipulandum to create a firm and rigid connection between the hand and the manilpulandum, or a custom fitted cast fit rigidly to the maniulandum that held the subject's wrist joint covering three-quarters of the forearm. The elbow was supported in a horizontal plane via a rope hanging from the ceiling. In [26], high resolution potentiometers were used to monitor the hand position in a horizontal plane. Voltage commands given to the motors were transformed into torques at the manipulandum's joint and finally to the end-effector forces. A similar manipulandum was constructed [10] used in [11] which incorporated cartesian-error-based inverse dynamics control approach to make the perturbation forces in various directions as uniform as possible. The manipulator consisted of a force sensor at the end-effector which was used to measure the restoring forces.

Acosta et. al [2] developed a robotic manipulator to create loads against which subjects perform various tasks and also to imposes stochastic perturbations onto the end-point of the arm to allow estimation of its mechanical properties given in [30]. The robot imposed stochastic position and force perturbations whose bandwidth exceeded that of the arm. These random perturbations avoid undesirable volitional reactions and allowed the efficient estimation of stiffness using experimental trials of short duration. In [37] the study

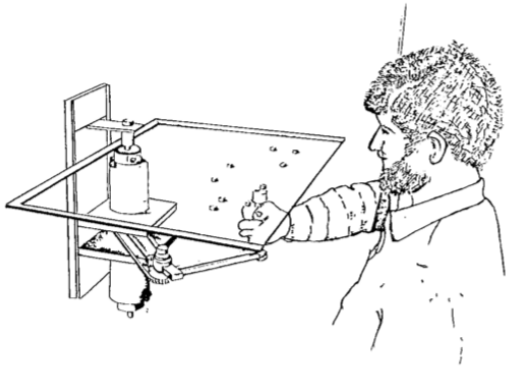

Figure 2.1: From [26] : Experimental setup for characterizing stiffness in a horizontal plane

was directed towards measuring both the static and dynamic characteristics of stiffness during multi-joint arm movement. This called for designing a manipulandum that needed to be (1) fast and light enough to minimize movement interference, while also being (2) strong enough to transmit large forces, and (3) rigid enough to be controlled at high frequencies. It was also possible to (4) support the human arm on a horizontal plane to be free from the force of gravity and to reduce fatigue. Additionally, (5) nonlinear forces due to manipulandum dynamics could be reduced so as not to disturb the arm movements. Details of this manipulandum is found in [37]. As shown in Fig. 2.2, during the static-stiffness experiments, force vector in the hori- zontal plane was displayed on a computer monitor. During the dynamic-stiffness experiments, the start and end positions, the target marker of the reference trajectory, and current handle position marker were displayed on the computer system.

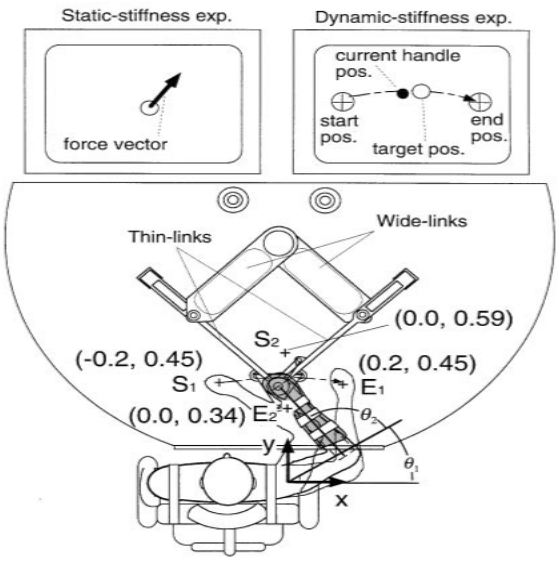


Figure 2.2: From [37] : The Parallel Link Drive Air-Magnet Floating Manipulandum (PFM) system and the experimental setup for measuring human arm stiffness. S and E respectively denote the start and end (posi-tions for the dynamic-stiffness experiments in the transverse movement) The origin of the axes is the shoulder position. On the computer monitor during the dynamic-stiffness experiments, the start and end positions, the target marker of the reference trajectory, and current handle position marker were displayed as shown in the top right of this figure. During the static-stiffness experiments, force vector in the hori- zontal plane was displayed on the computer monitor as shown in the top left of this figure.

## 2.3 Perturbation characteristics

As mentioned in 2.1, different displacement methods were employed in the various studies. In [26], the subjects were instructed to position the handle of the manipulandum that they have held with the right hand to five different locations in a horizontal plane as shown in Fig2.1. These five locations are within a rectangle of $280 \times 640mm$. Two high resolution potentiometers mounted on the axes of the mechanical joints were used to monitor the position of the hand. Two torque motors, connected independently to the two joints, measure the torques applied to manipulandum. Similar force regulation tasks were performed in [11] and [7]. Most of the studies conducted after these initial studies employed the method of applying stochastic perturbation to the hand of the subjects as shown in Fig

2.3

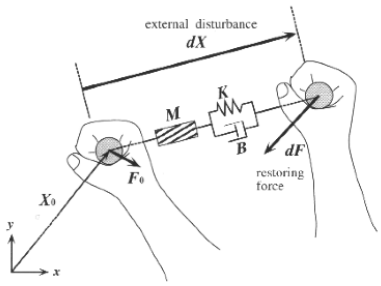


Figure 2.3: From [38] : Description of impedance model for small perturbations about an equilibrium point. While the subject maintains a specific hand location, a small external disturbance is applied to the hand

In [38] and [36] each perturbation had a pattern as shown in the figure which had an amplitude of 10*mm* and returned to the initial position in 400*ms*. In [37], the perturbation had trapezoidal profiles with an amplitude of $6-8mm$ in eight directions from the equilibrium point within 300*ms*. Five trials in each direction, randomly ordered, were recorded in one set for each of the five postural conditions. In [30] stochastic perturbations with peak-to-peak amplitudes of 20*mm* were applied. The displacement frequency content was designed within the range of physiologically encountered perturbations such as jerk, physiological tremor and low frequency drift but still contained enough information for adequate identification of end point dynamics. In all the above cases of stochastic perturbations, the amplitude and duration of the perturbations were small, allowing the constancy of either Inertia ($I$), Damping ($B$) or Stiffness ($K$). This also eliminated any significant influence of voluntary responses of the subjects on the measurements. Moreover, in order to avoid the prediction of either the onset of or directions of the perturbations, the perturbations were completely randomized.

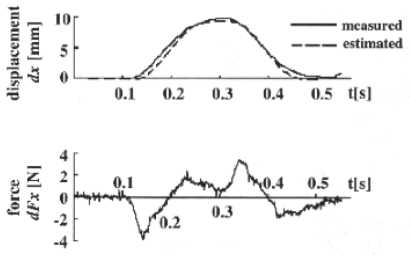


Figure 2.4: From [38] : Example of measured displacement and force profiles at the end-effector

Masia et. al [25] developed a mechanism conceived to measure multi-joint planar stiffness by a single measurement and in a reduced execution time. A mechanical rotary device that can apply cyclic perturbation to the human arm of known displacement and the force is acquired by means of a 6-axes commercial load cell. The unit mainly consists of a cam and planetary gear head that rotates at a controlled rpm. The subject is instructed to hold a handle attached to the cam. Through the rotation of the gear head, the hand is perturbed in 8 different directions from the center point as shown in the figure.

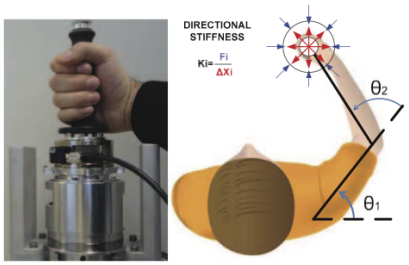


Figure 2.5: From [25] : Mechatronic device to measure end-point stiffness; Experimental setup showing the 8 directions of perturbation.

## 2.4 Impedance Estimation Technique

As seen in the previous sections 2.2 and 2.3, the impedance (starting with stiffness) characterizing technique for most of the studies were based off from the technique employed by Musaa-Ivaldi et. al [26]. They measured the position of the handle and the torques generated in the two motors and transformed them into positions and forces with respect to a reference frame at the subject' shoulder. Each of the two mechanical joints was controlled independently by using a linear position and velocity feedback law:

$$T' = a(\theta'_d - \theta'_a) - b(\dot{\theta}'_a) \tag{2.1}$$

where $T'$ is the controlled torque, $\theta'_d$ is the desired joint angle, $\theta'_a$ is the actual joint angle and $\dot{\theta}'_a$ is the actual angular velocity; $a$ and $b$ are the constant feedback gains.
The transformation from joint angles to the handle position ( in manipulandum reference system) is given by:

$$\begin{aligned} x' &= l'_1 cos(\theta'_1) + l'_2 cos(\theta'_1 + \theta'_2) \\ y' &= l'_1 sin(\theta'_1) + l'_2 sin(\theta'_1 + \theta'_2) \end{aligned} \tag{2.2}$$

where $l'_1$ and $l'_2$ are the manipulandum link lengths; $\theta'_1$ and $\theta'_2$ are, respectively, the manipulandum "shoulder" and "elbow" angles; and ($x'$,$y'$) are the coordinates of the handle.

The transformation from the torques to force is given by

$$\begin{aligned} F'_x &= \left[\frac{cos(\theta'_1+\theta'_2)}{l'_1} T'_1 - \frac{cos(\theta'_1)}{l'_2} T'_2\right] \cdot [sin(\theta'_2)]^{-1} \\ F'_y &= \left[\frac{sin(\theta'_1+\theta'_2)}{l'_1} T'_1 - \frac{sin(\theta'_1)}{l'_2} T'_2\right] \cdot [sin(\theta'_2)]^{-1} \end{aligned} \tag{2.3}$$

For small displacements about an equilibrium position, the imposed displacement and the

resulting forces are related by the following linear equations:

$$\begin{aligned} F_x &= -K_{xx}dx - K_{xy}dy \\ F_y &= -K_{yx}dx - K_{yy}dy \end{aligned} \tag{2.4}$$

The linear force-displacement relation may be written in the matrix form as

$$\begin{bmatrix} F_x \\ F_y \end{bmatrix} = \begin{bmatrix} K_{xx} & K_{xy} \\ K_{yx} & K_{yy} \end{bmatrix} \begin{bmatrix} dx \\ dy \end{bmatrix} \quad or \quad \mathbf{F} = \mathbf{K}\mathbf{dx} \tag{2.5}$$

The stiffness represented by the matrix $\mathbf{K}$ was separated into a symmetric component$\mathbf{K_s}$and an antisymmetric component $\mathbf{K_a}$ as follows:

$$\mathbf{K_s} = \begin{bmatrix} K_{xx} & (K_{xy}+K_{yx})/2 \\ (K_{yx}+K_{xy})/2 & K_{yy} \end{bmatrix} \tag{2.6}$$

$$\mathbf{K_a} = \begin{bmatrix} 0 & (K_{xy}-K_{yx})/2 \\ (K_{yx}-K_{xy})/2 & 0 \end{bmatrix} \tag{2.7}$$

noting that $\mathbf{K} = \mathbf{K_s} + \mathbf{K_a}$

Stiffness can be defined as a differentiable nonlinear function of the position for very small variations of force and with small displacements , i.e.,

$$\begin{aligned} dF_x &= \left(\frac{\partial F_x}{\partial x}\right) dx + \left(\frac{\partial F_x}{\partial y}\right) dy = K_{xx}dx + K_{xy}dy \\ dF_y &= \left(\frac{\partial F_y}{\partial x}\right) dx + \left(\frac{\partial F_y}{\partial y}\right) dy = K_{yx}dx + K_{yy}dy \end{aligned} \tag{2.8}$$

The above equation holds true for small displacements. The physical meaning of the symmetric impedance component is that the force field $f(x,y,z)$ is conservative. And the antisymmetric component represents the curl of the force field mainly generated by the subjects' hand.

Other studies [11], [29] and [38] have shown that under these postural conditions, a model with inertial ($I_E$), viscous ($B_E$), and elastic ($K_E$) terms can characterize the endpoint stiffness dynamics. For measurements in the horizontal plane, this mathematical model has the form given by:

$$[\mathbf{I}_E]\begin{bmatrix}\ddot{x}\\ \ddot{y}\end{bmatrix}+[\mathbf{B}_E]\begin{bmatrix}\dot{x}\\ \dot{y}\end{bmatrix}+[\mathbf{K}_E]\begin{bmatrix}x\\ y\end{bmatrix}=\begin{bmatrix}f_x\\ f_y\end{bmatrix} \tag{2.9}$$

where $\mathbf{I}_E$ is the inertia matrix defined by

$$\mathbf{I}=\begin{bmatrix}I_{xx} & I_{xy}\\ I_{yx} & I_{yy}\end{bmatrix} \tag{2.10}$$

$\mathbf{B}_E$ is the damping matrix defined by

$$\mathbf{B}=\begin{bmatrix}B_{xx} & B_{xy}\\ B_{yx} & B_{yy}\end{bmatrix} \tag{2.11}$$

$\mathbf{K}_E$ is the stiffness matrix defined by

$$\mathbf{K}=\begin{bmatrix}K_{xx} & K_{xy}\\ K_{yx} & K_{yy}\end{bmatrix}. \tag{2.12}$$

Gomi et. al. [37] applied stochastic perturbations while the subjects were instructed to move the handle of the manipulandum to four different points in a horizontal plane as shown in Fig 2.2. Accordingly to characterize stiffness, at first the two-link human arm dynamics on the horizontal plane were modeled given by the following second-order nonlinear differential equation:

$$\Psi(\ddot{\mathbf{q}},\dot{\mathbf{q}},\mathbf{q})=\tau(\dot{\mathbf{q}},\mathbf{q},\mathbf{u})=\tau_{\mathbf{ext}} \tag{2.13}$$

where $\Psi(\cdot)$ denotes the two-link arm dynamics and $\mathbf{q}$, $\dot{\mathbf{q}}$ and $\ddot{\mathbf{q}}$ are the angular position, velocity and acceleration vectors respectively. $\tau_{\mathbf{ext}}$ denotes the external force. Considering the length-tension and velocity-tension relationships of muscles forces, the generated torque, $\tau_{\mathbf{in}}$, can be represented as a function of angular position, velocity, and motor command $\mathbf{u}$ coming from the CNS. To estimate stiffness, viscosity, and inertia parameters by applying small perturbations, the following second order equation can be utilized:

$$\left(\frac{\partial\Psi}{\partial\ddot{\mathbf{q}}}\right)\delta\ddot{\mathbf{q}}+\left(\frac{\partial\Psi}{\partial\dot{\mathbf{q}}}\right)\delta\dot{\mathbf{q}}+\left(\frac{\partial\Psi}{\partial\mathbf{q}}\right)\delta\mathbf{q}=\left(\frac{\partial\tau_{\mathbf{in}}}{\partial\dot{\mathbf{q}}}\right)\delta\dot{\mathbf{q}}+\left(\frac{\partial\tau_{\mathbf{in}}}{\partial\mathbf{q}}\right)\delta\mathbf{q}+\delta\tau_{\mathbf{ext}} \tag{2.14}$$

If the arm is assumed to be a rigid body serial link system, modeled by :

$$\Psi(\ddot{\mathbf{q}},\dot{\mathbf{q}},\mathbf{q}) = \mathbf{I}(\mathbf{q})\ddot{\mathbf{q}} + \mathbf{H}(\dot{\mathbf{q}},\mathbf{q}) \tag{2.15}$$

and the muscle damping$(D)$ and joint stiffness$(R)$ $2\times 2$ matrices can be represented as:

$$\frac{\partial \tau_{\mathbf{in}}}{\partial \dot{\mathbf{q}}} \equiv \begin{bmatrix} D_{ss} & D_{se} \\ D_{es} & D_{ee} \end{bmatrix} \tag{2.16}$$

$$\frac{\partial \tau_{\mathbf{in}}}{\partial \mathbf{q}} \equiv \begin{bmatrix} R_{ss} & R_{se} \\ R_{es} & R_{ee} \end{bmatrix} \tag{2.17}$$

then eq. 2.14 can be written as

$$\mathbf{I}\delta\ddot{\mathbf{q}} + \frac{\partial \mathbf{H}}{\partial \dot{\mathbf{q}}}\delta\dot{\mathbf{q}} + \left(\frac{\partial \mathbf{I}\ddot{\mathbf{q}}}{\partial \mathbf{q}} + \frac{\partial \mathbf{H}}{\partial \mathbf{q}}\right)\delta\mathbf{q} = \mathbf{D}\delta\dot{\mathbf{q}} + \mathbf{R}\delta\mathbf{q} + \delta\tau_{\mathbf{ext}} \tag{2.18}$$

where $\mathbf{I}$ and $\mathbf{H}$ denote the inertial and coriolis-centrifugal force matrices respectively. The end point stiffness matrix $\mathbf{K}$ was obtained from joint stiffness matrix $\mathbf{R}$ as follows:

$$\mathbf{K} = (\mathbf{J}^T)^{-1}\left(\mathbf{R} + \frac{\partial \mathbf{J}^T}{\partial \mathbf{q}}\mathbf{F}_{in}\right)\mathbf{J}^{-1} \tag{2.19}$$

where $\mathbf{F}_{in}$ denotes force generated by the arm in Cartesian coordinates $(\mathbf{J}^T\tau_{in})$ and $\mathbf{J}$ denotes the Jacobian matrix of the kinematic transformation. The same force $\mathbf{F_{in}}$ is zero for static conditions without any external forces.

## 2.5 Impedance Representation and Results

Mussa-Ivaldi et. al [26] also introduced a way to represent the stiffness matrices derived as per section 2.4 using ellipses. As per [11] a concise graphical means of representing the symmetric component of such a matrix 2.6, is an ellipse 2.6, whose contour is the locus of force vectors produced by rotating a fixed length displacement vector or it's derivatives for other impedance components about the origin. Such an ellipse is characterized by size, shape and orientation. The size is propotional to the determinant, the shape is given by the ratio of the larger to the smaller eigenvalue and the orientation by the angle made by

the principal eigenvector with the x-axis. The larger and smaller eigenvalues are equal to the forces exerted along the major and minor axes, respectively, against a rotated unit displacement. If the eigenvalues are not equal to one another, i.e., if the contour is not a circle, it is only along these axes that the force is co-linear with the displacement.

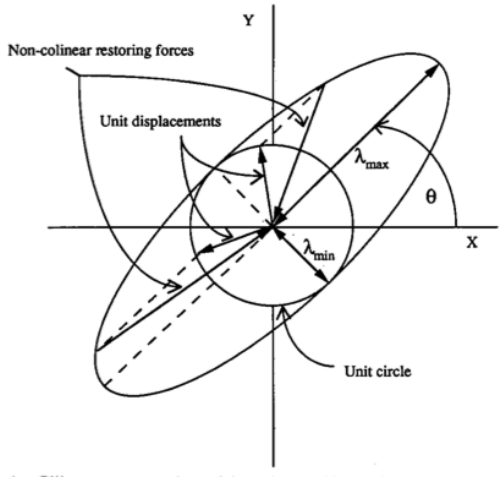


Figure 2.6: From [11] : Ellipse representation of impedance; $\lambda_{max}$ and $\lambda_{min}$ are the max and min eigenvalues of impedance matrices along principal and non-principal axes resp. $\theta$ shows the orientation of the ellipse

A similar approach was employed in [14] and [30]. From the end-point stiffness matrix **K** derived in eqn. 2.19, a stiffness ellipse was drawn to represent the direction and magnitude of elastic, resisting forces to a unit-length position perturbations in any direction. The major axis of the ellipse represents the maximum resisting force, which indicates the greatest stiffness. Conversely, the minor axis represents the minimum resisting force, indicating the least stiffness. To summarize the hand stiffness ellipse for each task, they used the major axis direction $\phi_e$ (or its relative angle to the shoulder-hand direction: $\phi_e - \phi_h$, its shape eccentricity $s$ ratio of the major and minor axis length), and size $A$ of the stiffness ellipse. In this case the parameter matrix was not required to be symmetric. $\lambda(\cdot)$ represented the eigenvalue operator.

$$\phi = tan^{-1}\left(\frac{U_{max_y}}{U_{max_x}}\right) \tag{2.20}$$

where $U_{max_x}$ and $U_{max_y}$ are obtained via singular value decomposition of the $\mathbf{K}$ matrix

$$\mathbf{K} = U \cdot S \cdot V^T, \quad U = \begin{bmatrix} U_{max_x} & U_{min_x} \\ U_{max_y} & U_{min_y} \end{bmatrix} \tag{2.21}$$

$$s = \frac{\alpha_{min}}{\alpha_{max}} \tag{2.22}$$

where $\alpha_{min} = \sqrt{\lambda_{min}(\mathbf{K}_{end}^T \cdot \mathbf{K}_{end})}$ and $\alpha_{max} = \sqrt{\lambda_{min}(\mathbf{K}_{end}^T \cdot \mathbf{K}_{end})}$

Area,

$$A = \pi \alpha_{min} \alpha_{max} \tag{2.23}$$

Stiffness values characterized by Mussa Ivaldi et. al. [26] using the formulation explained earlier in this subsection are given in Table.4.5 These are results for a particular subject(subject A) measured at five equilibrium points in the horizontal plane as shown in Fig. 2.1. The values are averaged over all the runs performed for each of the equilibrium points. Several observations are drawn from their data. First, at each work space location, the postural behavior is anisotropic; it has a strong directional character. There is a substantial difference between the major and the minor axes of the ellipses, i.e., between the minimum and the maximum stiffness. Second, the size, the shape, and the orientation of the stiffness ellipse all change with the position of the hand in the work space. It can be concluded that the end-point stiffness in work space coordinates is not an invariant quantity. However, in all their subjects, it was noted that the variations of shape and orientation followed a regular and repeatable pattern along the proximal-distal direction there is a predominant change in the ellipse shape, with a less pronounced change in orientation. The shape parameters indicate that when the hand was in the reference (equilibrium) position, the maximum stiffness was more than double the minimum stiffness. This anisotropy increased by a factor of two as the hand moved to the distal position. A slight, although, systematic clockwise rotation of the ellipse was observed when the hand posture changed from proximal to distal. In contrast the position changes going from left to right direction

resulted in a substantial rotation of the stiffness ellipse, with less pronounced changes in shape. The stiffness orientations changed by 15° between the proximal and distal positions, a rotation of more than 65° was observed between the right and left positions of the hand, with the major axis of the ellipse being approximately oriented towards the subject's shoulder. The observed changes in shape and orientations in with position in the work space were seen to be function of the geometric effects of the musculo-skeletal anatomy.

Table 2.1: From [26] : Arm end-point stiffness values for a subject measured for five different equilibrium points. *Units: N/m*

| Hand Position | $\overline{K}_{xx}$ $\overline{K}_{yx}$ | $\overline{K}_{xy}$ $\overline{K}_{yy}$ |
|---|---|---|
| Reference | -173± 7 | -387± 17 |
| | 27.4 ± 14 | -387±17 |
| Distal | -114± 5 | -641± 33 |
| | 24.1 ± 20 | -641±33 |
| Proximal | -251± 9 | -354± 19 |
| | 44.8 ± 17 | -354±19 |
| Right | -248 ± 18 | -409 ± 24 |
| | -207 ± 20 | -409±24 |
| Left | -450 ± 18 | -436 ± 21 |
| | 265 ± 22 | -436±21 |

Stiffness matrices taken from Table 2.1 were separated into the symmetric and anti-symmetric matrices as explained in eqn. 2.6 and eqn. 2.7 to find the corresponding representation using ellipses as shown in Fig. 2.7

As discussed in the previous section, Tsuji et. al [38] extended the characterization of impedance from stiffness, done by Mussa Ivaldi et. al [26], to characterizing inertia and damping along with stiffness. Their finding was that the the damping ellipses were approximately parallel to the the hand stiffness ellipses which had important implications in a control point of view. If the hand damping properties were fully isotropic and orthogonal to the hand stiffness, the dynamic behaviour of the hand motion would have different damping

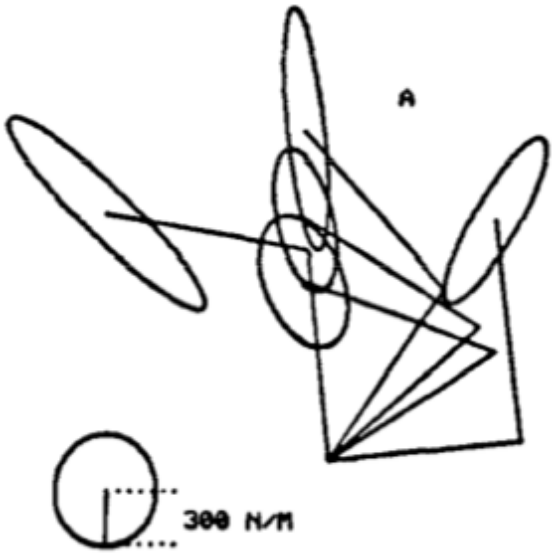


Figure 2.7: From [26] : Stiffness ellipses for data in Tab 2.1 for five different equilibrium points

characteristics in different movement directions which would be quite undesirable.

Table 2.2: From [38] : Arm end-point Stiffness values for subject A measured for four different equilibrium points. *Units: N/m*

| Hand Position | $\overline{K}_{xx}$<br>$\overline{K}_{yx}$ | $\overline{K}_{xy}$<br>$\overline{K}_{yy}$ |
|---|---|---|
| 1 | 105.72± 20.89 | -104.11± 14.75 |
| | -127.53± 31.67 | 234.78± 13.91 |
| 2 | 31.53± 9.81 | 41.36± 12.22 |
| | 13.38 ± 13.68 | 380.55 ± 61.94 |
| 3 | 232.77± 12.83 | -145.13 ± 20.12 |
| | -147.64 ± 8.169 | 173.38 ± 19.21 |
| 4 | 146.30± 36.34 | -63.43 ± 19.10 |
| | -61.26 ± 21.88 | 98.45 ± 23.21 |

The corresponding ellipses generated from Stiffness matrices from [38] for a particular subject (subject A) given in Table 2.2 respectively, is plotted in Fig. 2.8 below.

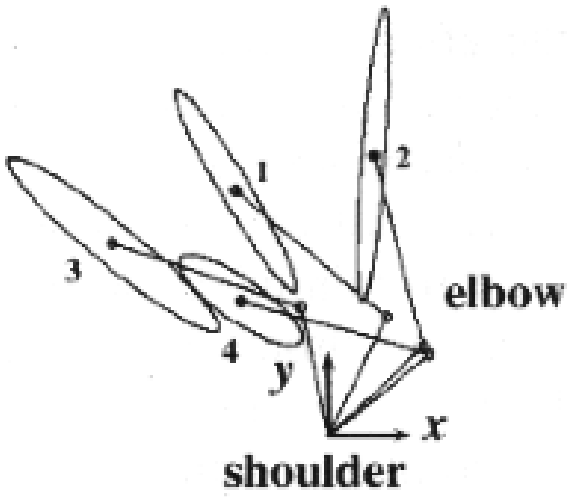


Figure 2.8: From [38] : Stiffness ellipses for data in Table 4.8 for four different equilibrium points

Inertia, damping and stiffness ellipses were generated by Dolan et. al [11] using the least-squared fitting experimental data and a two-cylindrical-link passive model of the human arm given by dashed lines and continuous line in the figures below.

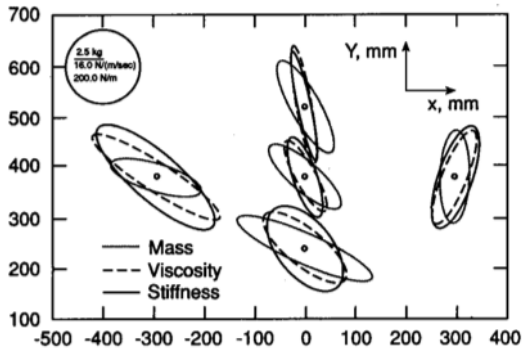


Figure 2.9: From [11] : Mass, damping and stiffness ellipses, for subject2. The radius of the calibration circle corresponds to $2.5kg$, $16Nm/s$ and $200N/m$ for the mass, damping and stiffness ellipses, respectively

## 2.6 Impedance Modulation

The first study on modulating impedance through muscle activation was reported by Mussa-Ivaldi et. al. [26] where they presented some observations of the stiffness ellipses through some force regulation techniques. The subjects were asked to maintain the hand at rest against an external destabilizing force. A force, of fixed direction and of sinusoidally varying amplitude, was imposed on the subjects' hand by the torque motors. The task was to maintain the hand at rest. After about 2 seconds, this force was removed and a servo displacement was applied (with a latency of about 1 set from the end of the oscillations) to measure the vectors used in the estimate of the stiffness. After the disturbance had been applied in brief pulses (30/ session) of 2 set duration, the stiffness of the hand was measured. Ellipses shown in Fig. 2.10 were obtained in three work-space positions: reference, right, and left. It was noted that the principal effect induced by all of the disturbances was a global increase in the magnitude of stiffness. The changes in shape and orientation were minimal compared with variations in size. They assumed that the strategy apparently adopted by humans was not to increase the stiffness selectively along the direction of the predictable disturbance, but to make the whole arm stiffer, presumably at the expense of a greater metabolic energy expenditure.

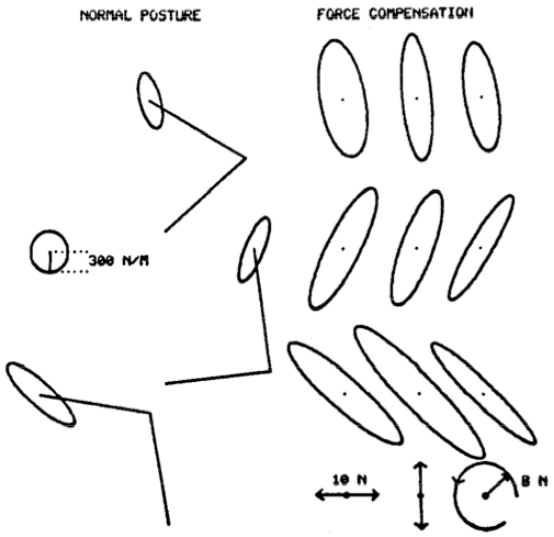


Figure 2.10: From [26] : Changes in stiffness induced by force compensation. The stiffness was measured during the compensation of a force acting along the x axis (left), a force acting along the y axis (middle), and a rotating force of constant amplitude (right)

Tsuji and Kaneko et. al. [36] conducted a study to estimate and model the human hand impedacne during muscle co-contraction for arm postures in a horizontal plane as an extension to their previous study in [38]. While subjects maintained a given hand location with a specified muscel activation level or a hand force, small disturbances were applied to the hand. During the experiment, surface EMG signal were measured from the following muscles:-

1. Pectoralis major
2. Infraspinatus
3. Brachialis
4. Triceps lateral head
5. Biceps Brachii
6. Triceps Brachii

After rectification and smoothing of the signal by second order Butterworth filter, the EMG signal measured from each muscle was normalized w.r.t the maximum voluntary contrac-

tion (MVC) of the muscle, which was defined as a muscle activation level $\alpha_i, i = 1,2,..6$ where $0.0 \leq \alpha \geq 1.0$.

The following conclusions were drawn from the study: (1) geometrical parameters of the hand stiffness and viscosity ellipses changed depending on the muscle activation levels of the subjects, (2) both the stiffness and the virtual equilibrium point of the subject's hand change depending on the amplitude of the generated hand force. (3) co-contraction of the flexor and the extensor increased the sizes of the hand stiffness ellipses. The estimated impedance characteristics of the human arm in their study showed a direction to provide basic and important data for complete modeling and analysis of the multi-joint human arm movements.

Gomi et. al [14] performed study to investigate how much joint stiffness could change under different conditions, and the effects of that on the spatial characteristics of the hand stiffness. Mainly, they investigated how different cocontraction ratios between the shoulder and elbow joints can produce changes in the shape and orientation of the stiffness ellipses. Their experimental setup was the same from [37] shown in 2.2. Additionally, rectified and filtered surface EMG of six muscles:-

1. Pectoralis major
2. Posterior deltoid
3. Brachioradialis
4. Lateral head of triceps brachii
5. Biceps brachii
6. Long head of triceps

were also displayed in a bar graph with an arbitrary scale. Reference EMG markers, representing desired EMG values for each task were established just before each experimental set and displayed as well. The subject was asked to keep his or her muscle activities constant at the reference markers throughout each experimental set.

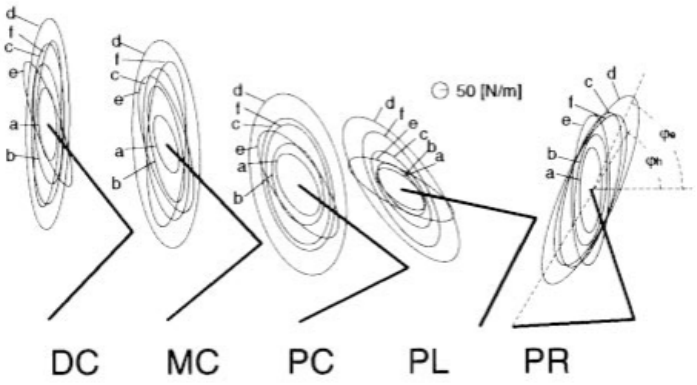


Figure 2.11: From [14] : Stiffness ellipses of a subject during posture maintenance tasks $(a-f)$ in five different postures (DC-distal center; MC-middle center; PC-proximal center; PL-proximal left; PR-proximal right). Each ellipse represents the stiffness during the requested task indexed by a roman character: (a) without cocontraction, (b) with quarter cocontraction, (c) half cocontraction, (d) full cocontraction, (e) cocontraction only in the shoulder, and (f) cocontraction only in the elbow

They noticed that in different tasks, the orientation and shape of the ellipses were altered as shown in Fig.2.11. In task $e$ (shoulder co-contraction) in all five postures, the orientations of the ellipses were rotated counterclockwise compared with those in other tasks, and the shoulder stiffness $(R_{ss})$ values were recorded to be higher than the elbow stiffness $(R_{ee})$ values. On the other hand, in task $f$, the orientations of ellipses, $\phi_e$, were similar to or smaller than those in task $d$, and the elbow joint stiffness values were recorded to be higher than the shoulder values in all five postures. Cross-joint stiffness values, $R_{se} and R_{es}$ from eqn.2.17, also increased in this task, whereas cross-joint stiffness values did not increase in task $e$. Also, in tasks $ad$ in the distal center, $bd$ in the middle-center, and $ad$ in the proximal center postures, the elbow joint stiffness values $(R_{ee})$ were higher than, or similar to, shoulder joint stiffness $(R_{ss})$. This tendency was frequently observed in the other three subjects as well. On the other hand, in tasks $a$ and $b$ in the proximal left posture and in task a in the proximal right posture, the shoulder joint stiffness values $(R_{ss})$ were higher than the elbow joint stiffness $(R_{ee})$. This may be caused by increases in shoulder flexor or extensor muscle activation to hold a left or right posture. By increasing the co-contraction level (tasks $c$ and $d$), however, the elbow joint stiffness $(R_{ee})$ exceeded the shoulder joint stiffness $(R_{ss})$.

# Chapter 3

# METHODOLOGY

This chapter presents the full framework designed for characterizing the regulation of human arm impedance through muscle co-contraction. Since the late 80's, there has been a substantial amount of interest in measuring human arm two dimensional (2D) end-point stiffness characteristics, where the arm is supported and constrained to movement within a horizontal (transverse) plane. A perturbation method for measuring hand stiffness was developed by using a manipulandum to displace the subject's hand during maintenance of a given posture in [26]. Stiffness values were represented both numerically and as ellipses (graphically). These showed that the human musculo-skeletal system has spring like properties that enable posture stabilization and interaction with the environment.

The perturbation method for estimating arm stiffness has been used by many other studies as well [7, 30, 31, 36]. In [11] and [38], the perturbation method was extended to include measurement of other dynamic components: inertia and damping in addition to stiffness. The first attempt to characterize arm impedance in three-dimensional (3D) space was described in [32]. However the stochastic methods used were not able to provide an insight into the neuromuscular system and its interaction with the environment.

Although most of the past studies have focused on perturbations during maintained hand posture, there are only a few studies that focused on the effect of muscle activation on the arm stiffness- again only on the horizontal (transverse) plane [13, 28, 36]. Since everyday tasks involve movement of the upper arm in the 3D space, this thesis illustrates the characterization of human arm impedance in this space and the how contribution of muscle co-contraction towards changing these characteristics is significant.

## 3.1 Experimental Setup

### *Introduction*

The subjects were seated on a chair placed next to a 7-DoF light weight robot arm (LWR4+) from KUKA robotics. They were strapped to the chair and their right arm was coupled to the robot arm via a mechanical coupling, attached to the end-effector of the robot arm as shown in Fig.3.1. The mechanical coupling is designed such that it allows no axial or rotational movement of the lower arm inside it, since it is attached to the human forearm close to the wrist [27]. The coupling insured that there was no kinematic redundancy in the subject's arm for any configuration. The mechanical coupling is capable of transmitting forces and torques in all directions between the robot and the coupled human arm. The robot arm position and force measurement accuracy is $0.01mm$ and $0.01N$ respectively, which were sufficient for the experiments of this study. An active motion capture system was used to track the motion of the arm, as well as compute the human arm configuration. Two reference systems were defined; one at the mounting plate of the robot arm $\langle X_B, Y_B, Z_B \rangle$, and the other at the shoulder of the human subject $\langle X, Y, Z \rangle$. The latter is defined so that the subject's torso coincides with the $X$-$Z$ plane and the vector joining the shoulders is parallel to the $Z$-axis. Finally, the $X$ axis is vertically oriented as shown in Fig.3.1.

### *Experimental Protocol*

Four subjects, all male ranging in age from 20 to 26 years similar in height and weight, three of them right handed and one left handed, participated in this experiment. As explained above, the subjects were strapped onto a seat placed next to the robot arm. Seven different end-effector poses (position and orientation) in the robot workspace were selected. With the subject strapped in the same position on the chair and their right hand coupled to the end-effector, each of these start points $S^{(i)} : i = 1, 2, .., 7$ corresponded to a specific configuration of the subject's arm. The seven arm configurations tested spanned a wide range of arm positions in 3D space, as shown in Fig. 3.2. The robot was controlled to impose

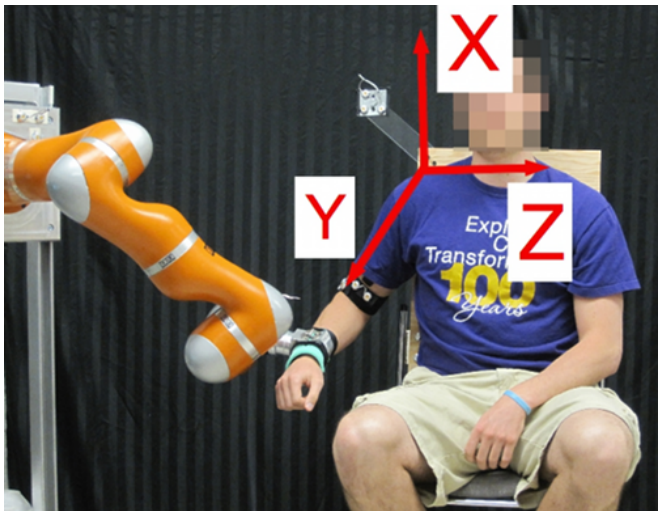


Figure 3.1: Experimental setup: The robot arm is interfaced with the subject's forearm through the mechanical coupling attached at the end-effector. Position tracking sensors are placed adjacent to the robot base and subject's shoulder defining two reference systems. EMG electrodes are placed on 6 muscles of the shoulder and elbow. Chair straps are not shown in the picture, but they were used during the experiments.

perturbations in 18 different directions in 3D space. This was done by controlling the robot to move to 18 equally-spaced points $P_j^{(i)}$, $j = 1,\ldots,18$ that lie on a sphere with a center of the corresponding $S^{(i)}$ point, and a radius of $8mm$. The motion of the robot from $S^{(i)}$ to one of the 18 $P_j^{(i)}$ points lasted $100ms$, and corresponded to the robot-induced perturbation to the human arm. Once the robot arrives at $P_j^{(i)}$, it remains stationary for $500ms$ and then returns back to $S^{(i)}$. After a resting phase of $1s$, the robot is commanded to reach the next $P_j^{(i)}$ point, and the procedure is repeated for all the 18 $P_j^{(i)}$ points.

The trajectory of the robot motion along each axis was designed using a 3rd order polynomial function. The trajectories were planned such that the orientation angles of the robot end-effector (roll, pitch, yaw) remained the same as those of the corresponding start points. The pseudo-inverse Jacobian method for solving the inverse kinematics of the robot arm was used offline [34]. Once the robot joint angle trajectories were computed, they were fed to the robot arm controller. The robot provided feedback of the joint angles, as well as end-effector forces at a frequency of $1000Hz$.

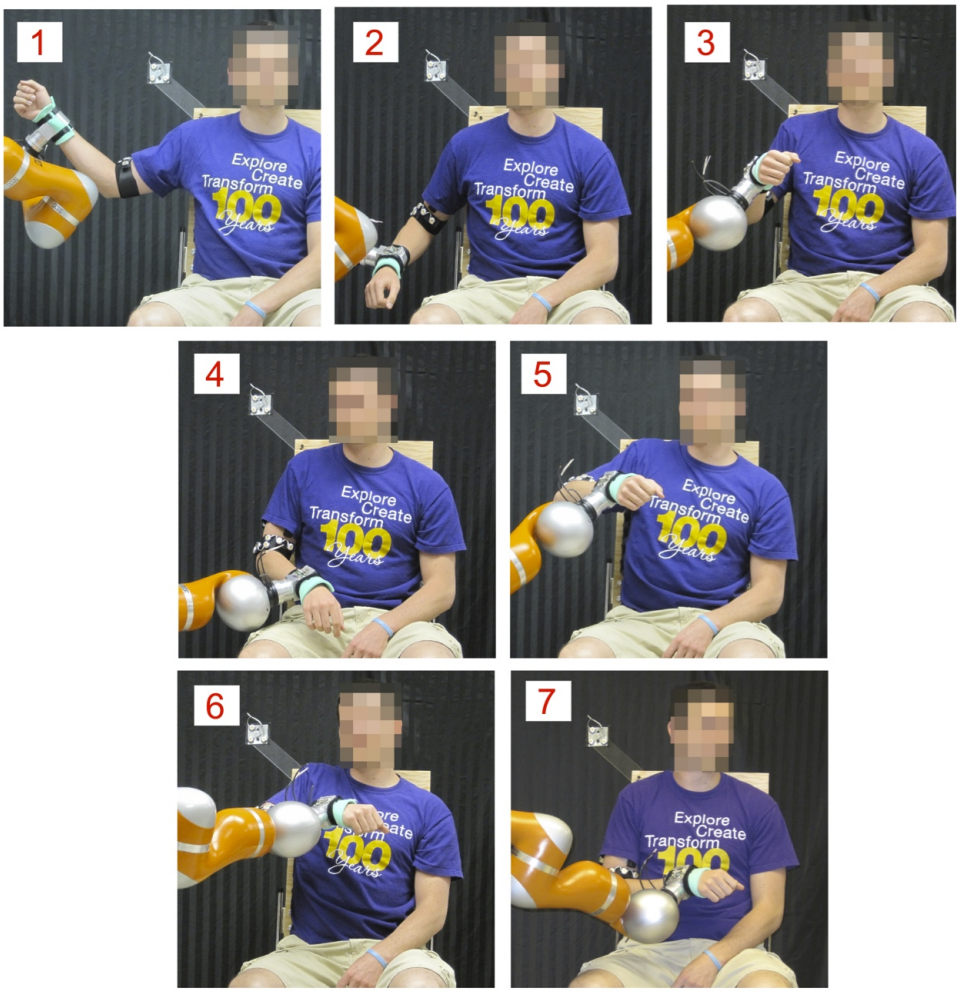


Figure 3.2: The 7 configurations of the arm used.

The robot-induced perturbation experiments were divided into four phases. In each phase, the subject was asked to maintain a certain co-contraction level of his/her muscles. The robot-induced perturbations were identical across the four phases. The co-contraction index $C$ was computed in real-time based on the muscles' activation, explained in detail in 3.2, and was displayed to the subject in the form of a bar graph, as shown in Fig. 3.10. The visual display was shown on a monitor placed in front of the subject, and was updated at a frequency of $1000Hz$. The levels of co-contraction asked of the subjects to maintain were 0%, 50%, 75% and 100% for the four phases respectively. For each of the 7 arm configurations, the robot perturbation phase was divided into three sets of 6 perturbations

each, thereby providing enough time for the subject to relax his/her muscles and limiting possible muscle fatigue.

*Robot Programming*

As explained in the previous subsection 3.1, the robot had a particular method of the perturbation i.e., the robot was programmed, in position control mode, to follow specific trajectories in each experiment. These trajectory files were generated offline in MATLAB. The process is explained in the block diagram in Fig. 3.3. The individual tasks involved are explained subsequently.

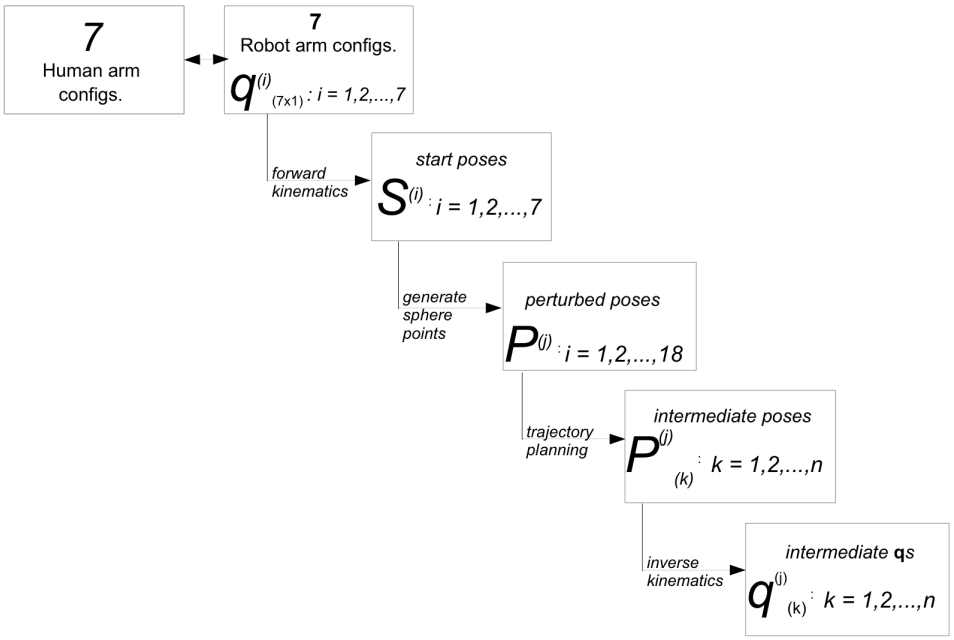


Figure 3.3: Block diagram showing how perturbation trajectory files were generated

Forward Kinematics of the robot arm

The forward kinematics of an open chain - serial link manipulator is a relation to compute the pose ( position and orientation ) of the end-effector as a function of the joint variables. This relation is established by first considering the description of a kinematic relationship between consecutive links and then to obtain an overall description of the manipulator in a recursive fashion. In robotics, the kinematic relationship is given using a homogeneous transformation matrix

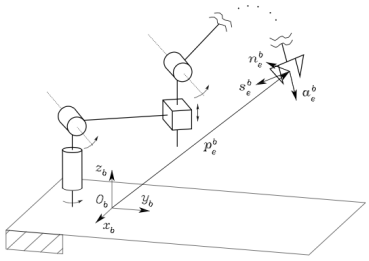


Figure 3.4: From [34] : Desription of the position and orientation of the end-effector frame

$$\mathbf{T}_e^b(\mathbf{q}) = \begin{bmatrix} \mathbf{n}_e^b(\mathbf{q}) & \mathbf{s}_e^b(\mathbf{q}) & \mathbf{a}_e^b(\mathbf{q}) & \mathbf{p}_e^b(\mathbf{q}) \\ 0 & 0 & 0 & 1 \end{bmatrix} \tag{3.1}$$

where $\mathbf{q}$ is the $(n \times 1)$ vector of joint variables, $\mathbf{n}_e$, $\mathbf{s}_e$, $\mathbf{a}_e$ are the unit vectors of frame attached to the end-effector, and $\mathbf{p}_e$ is the position vector of the origin of this frame w.r.t the base frame $O_b$

The Denavit-Hartenberg convention was adopted to generate the above mentioned homogeneous transformation matrices and the DH parameters for the robot arm used are shown in Table 4.5

Inverse Kinematics of the robot arm

The inverse kinematics of a serial link manipulator consists of determination of the joint variables corresponding to a given end-effector position and orientation. The inverse kine-

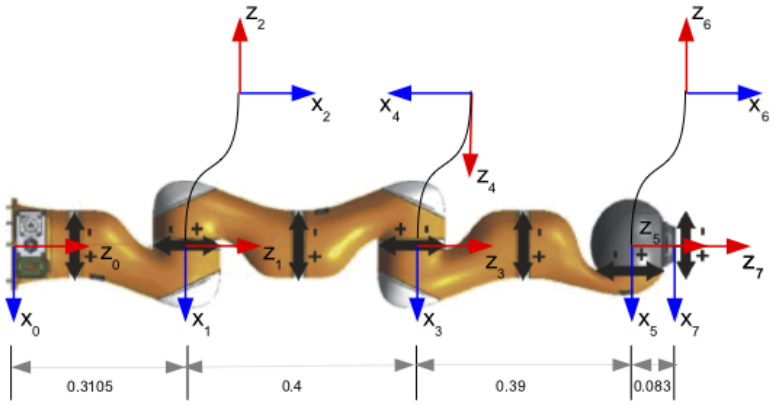


Figure 3.5: Links and frames assignment of the LWR4+. Dimensions are given in m. Image modified from [1]

Table 3.1: DH parameters for the KUKA LWR4+

| Link | $a_{i-1}$ (m) | $\alpha_{i-1}$ (rad) | $d_i$ (m) | $\theta_i$ (rad) |
|---|---|---|---|---|
| 1 | 0 | 0 | 0.3105 | $\theta_1$ |
| 2 | 0 | $\pi/2$ | 0 | $\theta_2$ |
| 3 | 0 | $-\pi/2$ | 0.4 | $\theta_3$ |
| 4 | 0 | $-\pi/2$ | 0 | $\theta_4$ |
| 5 | 0 | $\pi/2$ | 0.39 | $\theta_5$ |
| 6 | 0 | $\pi/2$ | 0 | $\theta_6$ |
| 7 | 0 | $-\pi/2$ | 0.083 | $\theta_7$ |

matics relation is of fundamental importance to transform end-effector motion into corresponding joint space motion that allow such motion to be executed. The LWR4+ is a kinematically redundant manipulator i.e., operational space variables, $r(=6)$ <DoFs, $n(=7)$. Hence there are infinite solutions to the inverse kinematics problem. The inverse Jacobian method was employed to solve the inverse kinematics which uses the differential kinematics equation to tackle the inverse kinematics problem. The use of differential kinematics results into an error in generating accurate joint velocities. The inverse kinematics algorithm is developed based on the block diagram shown in the Fig 3.6. The method establishes a relation between joint velocity vector $\dot{\mathbf{q}}$ and the error $\mathbf{e}$ using the *analytical*

Jacobian ($\mathbf{J}_A$), that ensures convergence of the error to zero. Thus joint angles $\mathbf{q}$ corresponding to a given end-effector pose $\mathbf{x}_d$ are computed more accurately. More details of the method can be found in [34]

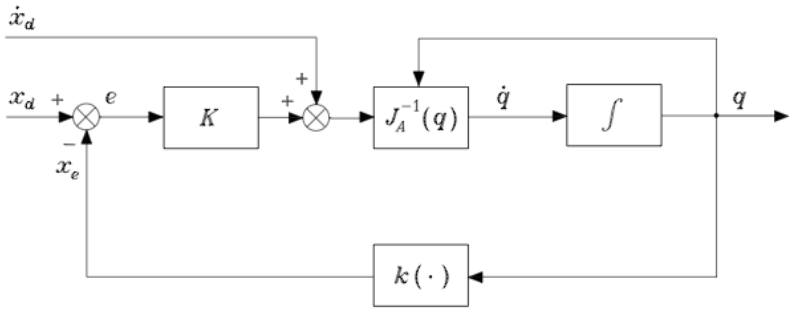


Figure 3.6: From [34]: Inverse kinematics algorithm with Jacobian inverse

## 3.2 EMG Processing

### *Introduction*

Electromyography (EMG) is an experimental technique concerned with the development, recording and analysis of myoelectric signals. Myoelectric signals, similar to electrical signals, are formed by physiological variations in the state of muscle fiber membranes. Besides basic physiological and biomechanical studies, EMG is established as an evaluation tool for applied research, physiotherapy/rehabilitation, sports training and interactions of the human body to industrial products and other work conditions. Besides answering the basic question, "what are the muscles doing?", EMG offers other benefits like allowing us to detect muscle response hence muscles responsible for for various movements, to measure muscular performance etc., allowing us to directly look into the muscles.

### *Physiological mechanism underlying EMG*

In the study of muscle physiology, neural control of excitable muscle fibres is explained on the basis of the action potential mechanism. The electrical model for the motor action potential reveals how EMG signals provide us with a quantitative, reliable, and objective means of accessing muscular information. Muscle fibres are composed of muscle cells that are in constant ionic equilibrium and also ionic flux. The semi-permeable membrane of each muscle cell forms a physical barrier between intracellular (typically negatively charged compared to external surface) and extracellular fluids, over which an ionic equilibrium is maintained. These ionic equilibriums form a resting potential at the muscle fibre membrane (sarcolemma), typically $-80$ to $-90mV$ (when not contracted). This potential difference is maintained by physiological processes found within the cell membrane and are called ion pumps. Ion pumps passively and actively regulate the flow of ions within the cell membrane. When muscle fibres become innervated, the diffusion characteristics on the muscle fibre membrane are briefly modified, and $Na^+$ flows into muscle cell membranes resulting in depolarization. Active ion pumps in the muscle cells immediately restore the

ionic equilibrium through the repolarization process which lasts typically $2-3ms$.

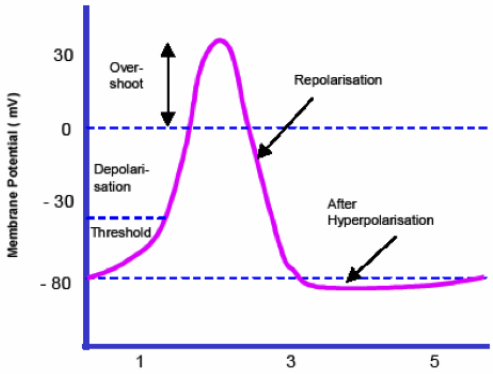


Figure 3.7: From [22] : The action potential within excitable membranes that are responsible for generating EMG signal

When a certain threshold level is exceeded by the influx of $Na+$ resulting in a depolarization of the cellular membrane, an action potential is developed and is characterized by a quick change from $-80mV$ to $+30mV$. This monopolar electrical burst is restored in the repolarization phase and is followed by a hyperpolarization period. Beginning from the motor end plates, the action potential spreads across the muscle fibres in both directions at a propagation speed of $2-6m/s$. The action potential leads to a release of calcium ions in the intra-cellular fluid and produces a chemical response resulting in a shortening of the contractile elements of the muscle cells.

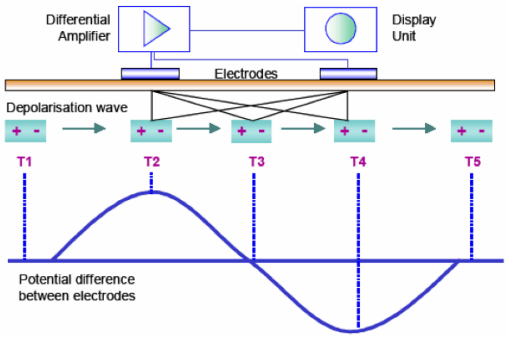


Figure 3.8: From [22] : An electrical model for the motor action potential

The depolarization-repolarization process described is a monopolar action potential that travels across the surface of the muscle fibre. Electrodes in contact with this wave

front present a bipolar signal to the EMG differential amplifiers because the electrodes are measuring the difference between two points along the direction of propagation of the wave front. EMG signals provide us with a viewing window into the electrical signals presented by multiple muscle fibres and are in fact a superposition of multiple action potentials.

*EMG acquisition and Muscle Co-Contraction Index*

Every joint in the human body is mobilized by the muscles that generate forces in opposing directions. Therefore, it is possible to control separately both the torque and the stiffness at the joint. The net torque at a joint is the difference between the torques of the agonist and antagonist muscle sets. The net stiffness is the sum of the individual stiffness of the agonist and antagonist muscle sets. Thus the value of these two variables may range from high torque and low-stiffness, when either the agonist set or antagonist set is individually activated, to zero torque and high stiffness when both are co-activated. By muscle co-contraction (simultaneously activating antagonist muscles around a joint), the CNS can tune the mechanical properties of the limb in response to task requirements both in holding posture and during limb movements [15]. Changes in muscle cocontraction affect joint impedance, which provides mechanical stability in the presence of external perturbations and forces due to limb dynamics. Behavioral studies of limb postural control have shown that humans are able to modulate the co-activation of antagonist muscles i.e. co-contract muscles, around multiple joints to minimize the perturbing effects of external loads when interacting with the environment. Increases in joint stiffness brought about by muscle co-contraction would have a beneficial effect on limb stability and hence movement and interaction accuracy. Gomi et. al. [14] conducted their study investigating how different co-contraction ratios between the shoulder and elbow joints can produce changes in the stiffness ellipsoids explained in section 2.5. Following all these previous studies, the framework presented in this thesis involves studying how humans can regulated the arm impedance through the co-contraction of the muscles of shoulder and elbow joint simultaneously. The muscles selected for this study were:

1. Anterior deltoid. - *forward flexion, medial rotation, adduction*
2. Posterior deltoid - *extension, lateral rotation, and abduction*
3. Pectoralis major - *horizontal adduction*
4. Trapezius - *adduction, upward rotation*
5. Biceps brachii - *forearm flexion, supination*
6. Long head of triceps brachii - *forearm extension*

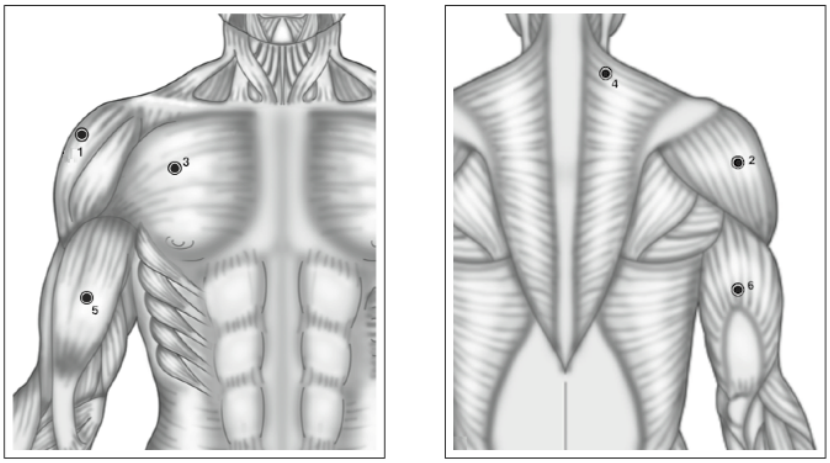


(a) Anterior side (b) Posterior side

Figure 3.9: Placement of EMG surface electrodes in six muscles: (1) anterior deltoid, (2) posterior deltoid, (3) pectoralis major (4) trapezius, (5) biceps brachii, (6) long head of triceps; fig. from [9] (modified)

In the experiment, individual EMG signals were acquired from the six muscles and processed to produce an index that can represent the magnitude of muscle co-contraction. The individual muscle activation was recorded using Trigno Wireless EMG System. Each Trigno Sensor is equipped with the following features:

1. transmission range of $40m$
2. inter-sensory latency $<500\mu s$
3. EMG signal badwith $20-450$ Hz
4. EMG baseline noise of $<750nV$ RMS
5. $16-$bit EMG signal resolution

Prior to performing the experiment, the subjects were asked to co-contract their arm muscles to their maximum ability, while their arm was in one of the 7 configurations selected (configuration 5). EMG signals were recorded from the six muscles mentioned above and sampled at a frequency of $1000Hz$. The signals were then full-wave rectified and low-pass filtered (2nd order Butterworth filter, cut-off frequency of 8 Hz). The processed signals $e_m, m = 1,\ldots,6$ were stored, and the maximum values for each muscle $e_{m,\max}$ were recorded to be used as a normalization factor for the experiments. During the perturbation experiments the total co-contraction index $C$ was computed in real-time based on the individual muscle normalized activation level with respect to their maximum activation level $e_{m,\max}$. Therefore, the co-contraction index was given by:

$$C = \frac{1}{6}\sum_{m=1}^{6}\frac{e_m}{e_{m,\max}} \tag{3.2}$$

The co-contraction index $C$ was computed in real-time based on the muscles' activation. A simple visual display was designed in OpenGL®which featured a bar graph that changed in height based on the value of the co-contraction index. The visual display directed the subject to maintain the specific co-contraction level for that particular phase, as shown in Fig. 3.10. The visual display was shown on a monitor placed in front of the subject, and was updated at a frequency of $1000Hz$.

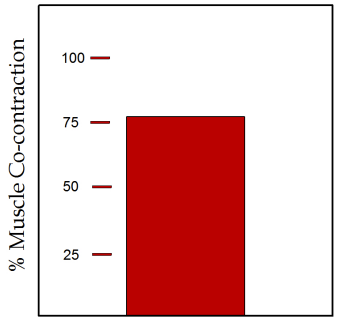


Figure 3.10: Visual display indicating the muscle co-contraction index.

# Chapter 4

# DATA ANALYSIS AND RESULTS

## 4.1 Data Processing

As explained earlier, the goal of the study is to investigate how the arm impedance changes as a function of muscle co-contraction. The arm impedance characteristics - inertia, damping and stiffness - are characterized using a linear model describing the relationship between measured restoring forces and position of the arm.

In the experiment, the arm is coupled to the end-effector of the robot arm via the mechanical coupling. The position of the end point of the arm, a point in the forearm, was defined as the center point of the cylindrical housing of the mechanical coupling. Since the coupling was attached to the robot arm, the 3D position of this point was tracked at each instance through the robot joint angles after applying the forward kinematic equations of the robot arm. Therefore, all the motion profiles and end-effector forces were obtained with respect to the robot base reference system $\langle X_R, Y_R, Z_R \rangle$. Using homogeneous transformation between the robot and the robot mounting plate reference system $\langle X_B, Y_B, Z_B \rangle$, the position of the human end-point, and the interaction forces, were computed with respect to the human-centered reference frame $\langle X, Y, Z \rangle$

*Impedance Estimation in 3D Space*

The force and motion profiles of interest, i.e. during the $100ms$ robot-induced perturbations, were extracted for processing. The initial values of forces in all directions were first subtracted from the subsequent force profiles. This ensured that any kind of sensor offset or gravitational forces due to weight of the arm didn't affect the restoring force measurements. Since length and duration of the perturbations was very small, the model of the end point impedance can be expressed by the following equation:

$$\mathbf{F} = \mathbf{I}\ddot{\mathbf{X}} + \mathbf{B}\dot{\mathbf{X}} + \mathbf{K}\mathbf{X} \tag{4.1}$$

where **I**, **B** and **K** represent the $3 \times 3$ arm inertia, damping and stiffness matrices respectively. $\ddot{\mathbf{X}}$, $\dot{\mathbf{X}}$ and **X** are the 3D acceleration, velocity and displacement vectors respectively, while **F** is the 3D vector of restoring forces. All variables are expressed with respect to the human-centered reference system $\langle X, Y, Z \rangle$. Equation (4.1) can be re-written in a parameter identification form as shown below:

$$\mathbf{F} = \mathbf{P}\mathbf{y} \tag{4.2}$$

where $\mathbf{F} = [F_x \quad F_y \quad F_z]^T$, $\mathbf{y} = [\ddot{\mathbf{X}}^\mathbf{T} \quad \dot{\mathbf{X}}^\mathbf{T} \quad \mathbf{X}^\mathbf{T}]^T$ and **P** is a $3 \times 9$ impedance matrix to be identified, given by

$$\mathbf{P} = [\mathbf{I} \quad \mathbf{B} \quad \mathbf{K}] \tag{4.3}$$

where **I** is the inertia matrix defined by

$$\mathbf{I} = \begin{bmatrix} I_{xx} & I_{xy} & I_{xz} \\ I_{yx} & I_{yy} & I_{yz} \\ I_{zx} & I_{zy} & I_{zz} \end{bmatrix} \tag{4.4}$$

**B** is the damping matrix defined by

$$\mathbf{B} = \begin{bmatrix} B_{xx} & B_{xy} & B_{xz} \\ B_{yx} & B_{yy} & B_{yz} \\ B_{zx} & B_{zy} & B_{zz} \end{bmatrix} \tag{4.5}$$

**K** is the stiffness matrix defined by

$$\mathbf{K} = \begin{bmatrix} K_{xx} & K_{xy} & K_{xz} \\ K_{yx} & K_{yy} & K_{yz} \\ K_{zx} & K_{zy} & K_{zz} \end{bmatrix}. \tag{4.6}$$

Using $n$ number of data points for restoring force and position measurements collected from the experiments, the impedance matrix $P$ was computed using linear regression method given by the following:

$$\mathbf{P} = \mathbf{F}_N \mathbf{Y}_N^\dagger \tag{4.7}$$

where $\mathbf{Y}_N^{\dagger}$ is the left pseudo-inverse matrix of $\mathbf{Y}_N$. $\mathbf{F}_N$ and $\mathbf{Y}_N$ were computed by concatenating $n$ instances of $\mathbf{F}$ and $\mathbf{y}$ respectively as follows:

$$\mathbf{F}_N = [\mathbf{F}_1 \cdots \mathbf{F}_n] \tag{4.8}$$

$$\mathbf{Y}_N = [\mathbf{Y}_1 \cdots \mathbf{Y}_n] \tag{4.9}$$

The impedance matrices $\mathbf{I}$, $\mathbf{B}$ and $\mathbf{K}$ were separated into symmetric and antisymmetric matrix components. Generally any $3 \times 3$ matrix $\mathbf{Z}$ can be separated into the symmetric $Z^{(S)}$ and anti-symmetric component $Z^{(A)}$ as follows:

$$\mathbf{Z} = \begin{bmatrix} Z_{xx} & Z_{xy} & Z_{xz} \\ Z_{yx} & Z_{yy} & Z_{yz} \\ Z_{zx} & Z_{zy} & Z_{zz} \end{bmatrix} = \mathbf{Z}^{(S)} + \mathbf{Z}^{(A)} \tag{4.10}$$

where

$$\begin{aligned} \mathbf{Z}^{(S)} &= \frac{1}{2}(\mathbf{Z} + \mathbf{Z}^T) \\ \mathbf{Z}^{(A)} &= \frac{1}{2}(\mathbf{Z} - \mathbf{Z}^T) \end{aligned} \tag{4.11}$$

Finally, if $f(x,y,z)$ is a differentiable, non-linear function of the position of the arm end-point, where $x,y,z$ is the position of the end point in 3D space, it is possible to express the end point impedance of the arm as a differential operator that relates small variations of force $(dF_x, dF_y, dF_z)$ to small displacements $(dx, dy, dz)$, i.e.

$$\begin{aligned} dF_x &= \left(\frac{\partial F_x}{\partial x}\right) dx + \left(\frac{\partial F_x}{\partial y}\right) dy + \left(\frac{\partial F_x}{\partial z}\right) dz \\ &= Z_x x d_x + Z_x y d_y + Z_x z d_z \\ dF_y &= \left(\frac{\partial F_y}{\partial x}\right) dx + \left(\frac{\partial F_y}{\partial y}\right) dy + \left(\frac{\partial F_y}{\partial z}\right) dz \\ &= Z_y x d_x + Z_y y d_y + Z_y z d_z \\ dF_z &= \left(\frac{\partial F_z}{\partial x}\right) dx + \left(\frac{\partial F_z}{\partial y}\right) dy + \left(\frac{\partial F_z}{\partial z}\right) dz \\ &= Z_z x d_x + Z_z y d_y + Z_y z d_z \end{aligned} \tag{4.12}$$

The above equation holds true for small displacements. Therefore the physical meaning of the symmetric impedance component is that the force field $f(x,y,z)$ is conservative. And the anti-symmetric component represents the curl of the force field mainly generated by the subjects' hand [26].

*Muscular Co-Contraction*

Before analyzing the impedance characteristics identified for the various levels of muscle co-contraction, it is worth investigating the ability of the human subjects to control their muscles' activation, based on the visual feedback of the co-contraction index introduced above. Fig. 4.1 shows the co-contraction index as calculated in three phases of the experiment, in which the subject was instructed to maintain it at 50%, 75% and 100% level respectively. The co-contraction index was defined with respect to maximum voluntary co-contraction in a *single* arm configuration. Configuration 5 was selected because it was approximately in the mid-range of the 3D arm workspace we used. There are two observations that can be drawn from the figure. Firstly, it can be seen that the subject was able to maintain the specific level of muscle co-contraction in each phase. Secondly, these indexes were seen to slightly vary across the 7 configurations indicating that the ability to co-contract the muscles to the specific level of co-contraction was different for different arm configurations. Although we could use maximum voluntary co-contraction for each configuration tested, we decided to use only one in order to have a more general idea of the muscle co-contraction level, that could generalize across configurations.

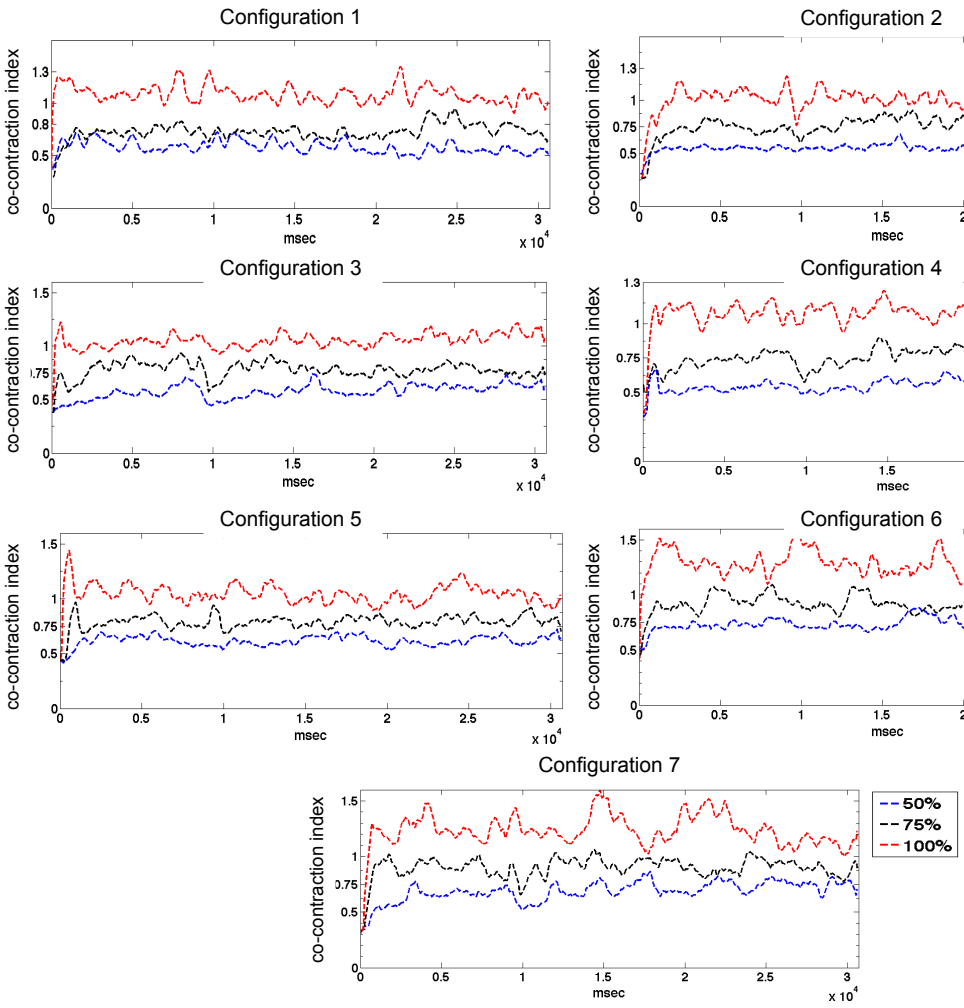


Figure 4.1: Co-contraction index $C$ for three muscle co-contraction levels 50%, 75% and 100%. A similar trend of maintaining the co-contraction index was seen for all the subjects.

Individual muscles EMGs were also analyzed to get a better understanding of the mechanism underlying muscle co-contraction. The EMG of a representative subject across the 4 levels of co-contraction are compared for two configurations (2 and 7) in Fig.4.2. It can be seen from the EMGs for configuration 2, that the posterior deltoid, trapezius and the triceps are the set of muscles that contributed to the co-contraction majorly. While in configuration 7 it is the anterior deltoid and pectoralis major muscles. Looking at the way the arm is configured 3.2, the length of these muscles are less than their respective resting length. According to the force to muscle length relation of the Hill muscle model, the

muscles produce a higher force when the length of the muscle is less than the resting length. Thus muscle co-contraction level across configurations possibly depends on the state of the individual muscles that governs it's ability to produce force in each configuration. The variability in this level indicates that the ability of an individual muscle to contribute to co-contraction is configuration dependent.

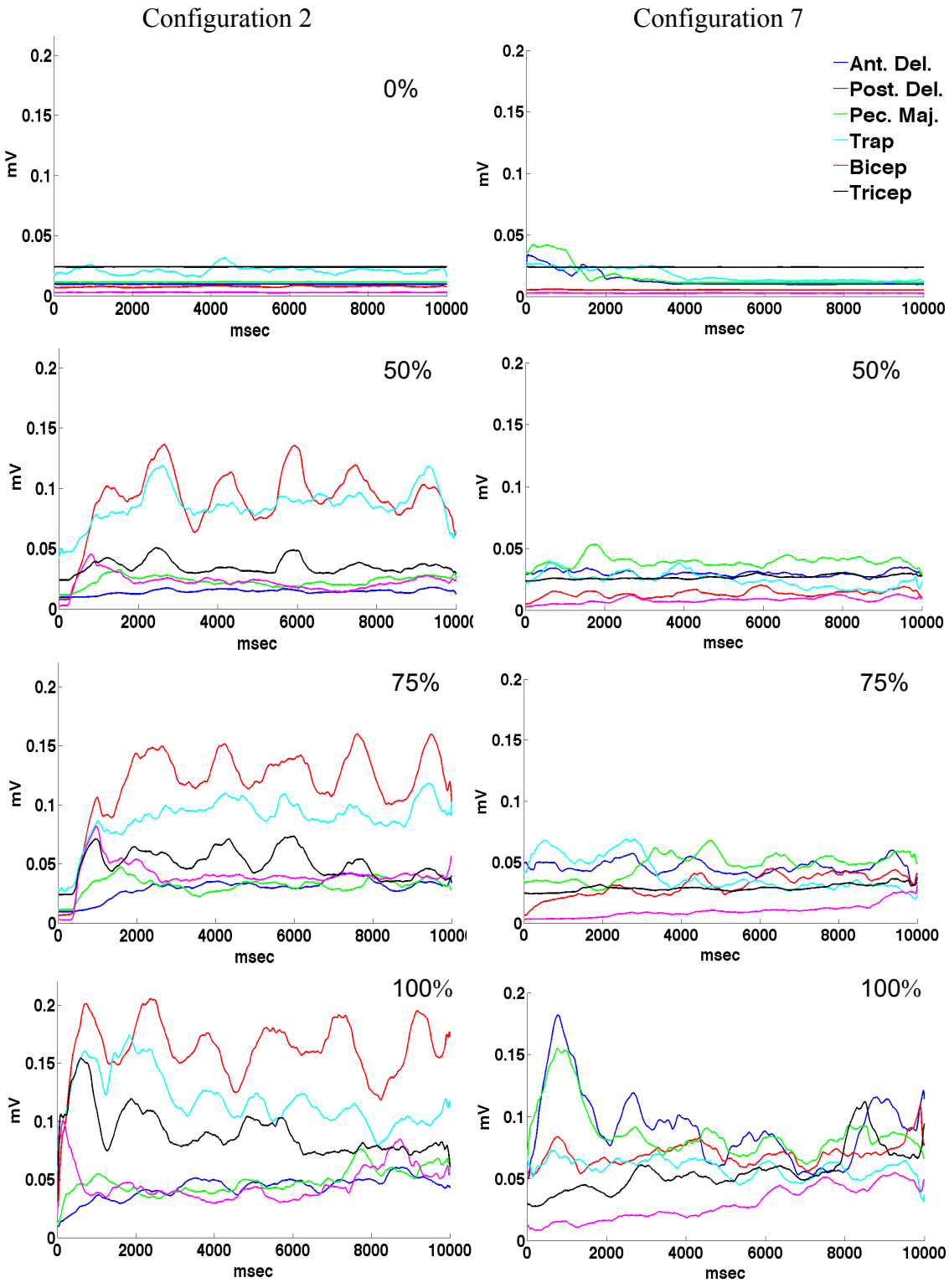


Figure 4.2: Comparision of individual muscle EMGs of a representative subject across all levels of co-contraction for configuration 2 (*left*) and 7 (*right*).

*Impedance matrices*

The impedance matrices $I$, $B$ and $K$ for each of the arm configurations were identified and separated into the symmetric and anti-symmetric components as described in section 4.1. It was observed that the restoring forces due to inertia ($I$) and damping ($B$) were very small compared to the ones due to arm stiffness, especially in the cases involving muscle co-contraction. For that reason, it is not certain that they were accurately identified using the least-squares equation. Moreover, the inertia of the arm is not expected to vary for different muscle co-contraction levels. If needed the inertia can be estimated for a static case using bio-mechanic analysis. There is no evidence from any background literature that damping would also change with muscle co-contraction, especially given isometric conditions we investigate here.

The diagonal elements of the identified arm stiffness $\overline{K}_{xx}$, $\overline{K}_{yy}$, $\overline{K}_{zz}$, averaged across all subjects, are listed in Tables 4.5, 4.6, 4.7, 4.8 for the different co-contraction levels 0%, 50%, 75% and 100% respectively. Moreover, the maximum of all off-diagonal elements of the anti-symmetric components $\overline{K}_{max_A}$ are also listed. It can be noted that the anti-symmetric components of stiffness are comparatively low.

Table 4.1: Arm stiffness characteristics for 0% co-contraction, averaged across all subjects.

| Configuration # | $\overline{K}_{xx}$ (N/m) | $\overline{K}_{yy}$ (N/m) | $\overline{K}_{zz}$ (N/m) | $\overline{K}_{max_A}$ (N/m) |
|---|---|---|---|---|
| 1 | 580.7 | 1082.0 | 1439.5 | 348.7 |
| 2 | 269.6 | 2405.1 | 873.4 | 507.2 |
| 3 | 455.8 | 2357.3 | 739.1 | 370.3 |
| 4 | 862.8 | 1735.2 | 583.1 | 136.8 |
| 5 | 667.3 | 2158.9 | 509.2 | 344.5 |
| 6 | 458.7 | 2904.9 | 654.1 | 163.5 |
| 7 | 684.9 | 2314.8 | 764.3 | 401.4 |

Table 4.2: Arm stiffness characteristics for 50% co-contraction, averaged across all subjects.

| Configuration # | $\overline{K}_{xx}$ (N/m) | $\overline{K}_{yy}$ (N/m) | $\overline{K}_{zz}$ (N/m) | $\overline{K}_{max_A}$ (N/m) ) |
|---|---|---|---|---|
| 1 | 651.1 | 1177.1 | 1674.6 | 290.5 |
| 2 | 559.9 | 2435.1 | 1021.5 | 492.4 |
| 3 | 524.1 | 2406.1 | 829.1 | 378.8 |
| 4 | 973.4 | 1766.3 | 654.6 | 113.3 |
| 5 | 799.4 | 2243.3 | 613.4 | 356.6 |
| 6 | 630.2 | 2927.0 | 775.6 | 213.1 |
| 7 | 944.5 | 2432.1 | 900.8 | 375.1 |

Table 4.3: Arm stiffness characteristics for 75% co-contraction, averaged across all subjects.

| Configuration # | $\overline{K}_{xx}$ (N/m) | $\overline{K}_{yy}$ (N/m) | $\overline{K}_{zz}$ (N/m) | $\overline{K}_{max_A}$ (N/m) |
|---|---|---|---|---|
| 1 | 451.8 | 1078.3 | 2144.3 | 293.3 |
| 2 | 620.5 | 2516.1 | 1004.6 | 475.6 |
| 3 | 602.7 | 2424.6 | 877.3 | 337.3 |
| 4 | 987.5 | 1773.2 | 709.7 | 122.9 |
| 5 | 790.2 | 2278.1 | 608.3 | 354.4 |
| 6 | 676.8 | 2968.0 | 826.7 | 219.1 |
| 7 | 1026.1 | 2441.9 | 943.2 | 350.8 |

Table 4.4: Arm stiffness characteristics for 100% co-contraction, averaged across all subjects.

| Configuration # | $\overline{K}_{xx}$ (N/m) | $\overline{K}_{yy}$ (N/m) | $\overline{K}_{zz}$ (N/m) | $\overline{K}_{max_A}$ (N/m) |
|---|---|---|---|---|
| 1 | 595.9 | 1149.8 | 1985.1 | 318.1 |
| 2 | 718.9 | 2502.8 | 1148.4 | 470.7 |
| 3 | 641.9 | 2423.5 | 844.2 | 334.4 |
| 4 | 1076.9 | 1830.9 | 728.3 | 114.2 |
| 5 | 831.3 | 2371.6 | 660.6 | 379.3 |
| 6 | 725.3 | 3002.6 | 788.4 | 232.1 |
| 7 | 1167.8 | 2476.4 | 915.5 | 339.6 |

## 4.2 Impedance Representation in 3D

The symmetric components of the stiffness matrices give a representation of a spring system in 3-dimension as shown in Fig.. The diagonal elements of the matrix $K_{xx}$, $K_{yy}$, $K_{zz}$ are the individual spring stiffness values along $X-$, $Y-$ and $Z-$ axis of the human-centered reference frame $\langle X,Y,Z\rangle$. The bar plots shown in Fig.4.3, Fig.4.4 and Fig.4.5 present a comparison of the stiffness values along these directions for the 4 subjects across all the 7 configurations. It is seen that stiffness values for the 4 subjects fall in a similar range since all the subjects are anthropometrically similar i.e. similar in height and weight, validating the estimation method. Moreover a similar trend of change in stiffness values along the 3 directions across the 7 configuration is seen. Among the 3 directions, for each configuration there is a primary axis along which the stiffness values is the highest compared to the other axes. The line joining the distal end of the arm with the shoulder is always along this primary axis.

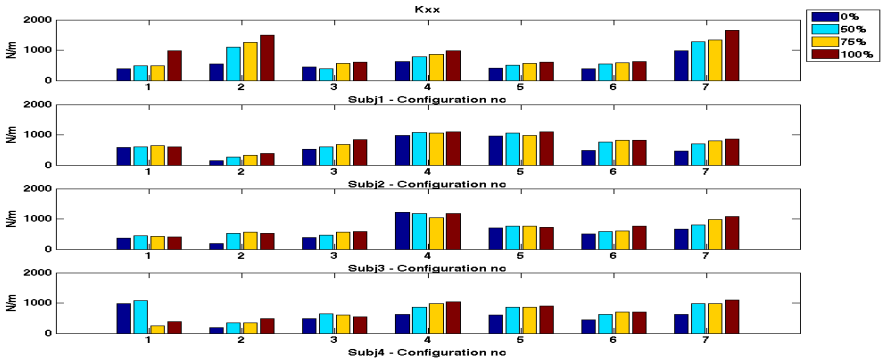


Figure 4.3: Bar plot comparing stiffness values in $X-$ direction at 0%, 50%, 75% and 100% muscle co-contraction levels for the 4 subjects across the 7 configurations

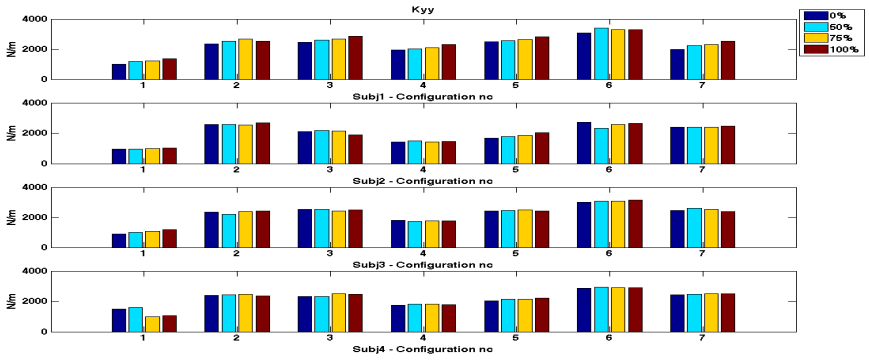


Figure 4.4: Bar plot comparing stiffness values in $Y-$ direction at 0%, 50%, 75% and 100% muscle co-contraction levels for the 4 subjects across the 7 configurations

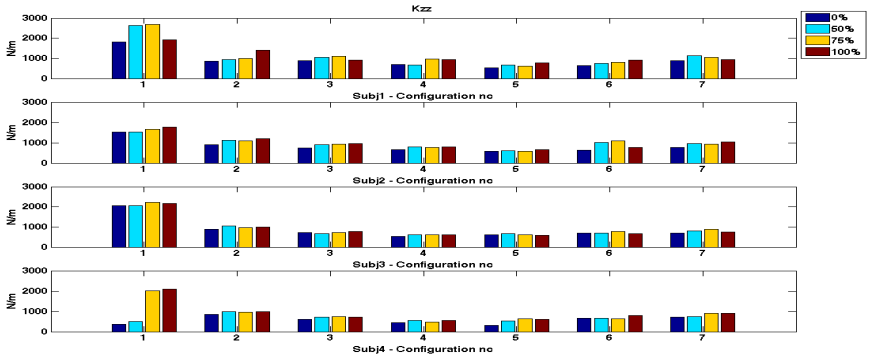


Figure 4.5: Bar plot comparing stiffness values in $Z-$ direction at 0%, 50%, 75% and 100% muscle co-contraction levels for the 4 subjects across the 7 configurations

## 4.3 Impedance Representation Using Ellipsoids

The study in this thesis is directed to investigating how the 3D impedance characteristics are regulated through muscle co-contraction. This regulation is also arm configurations dependent as seen from the bar graphs plotted in section 4.2. A representation of the impedance that gives a more elaborative picture of the changes for small changes in configuration and muscle co-contraction is thus required. Use of ellipsoids with it's geometric characteristics presents the required representation. These characteristics include shape, size and orientation of the ellipsoid. The shape of the ellipsoid is indicative of the directions of highest and lowest stiffness. A change in size of the ellipsoid is indicative of the change in the stiffness

for any direction for changing co-contraction levels while the orientation is indicative of any change in direction of these axes for either a configuration change or co-contraction level change.

An ellipsoid centered at the origin is represented by the following equation:

$$a_{11}x^2 + a_{22}y^2 + a_{33}z^2 + 2a_{12}xy + 2a_{13}xz + 2a_{23}yz = 1 \tag{4.13}$$

where $a_{11}, a_{22}, a_{33}, a_{12}, a_{13}, a_{23}$ are elements of a symmetric $3 \times 3$ matrix $\mathbf{A}$, i.e

$$\mathbf{A} = \begin{bmatrix} a_{11} & a_{12} & a_{13} \\ a_{12} & a_{22} & a_{23} \\ a_{13} & a_{23} & a_{33} \end{bmatrix} \tag{4.14}$$

The principle axes of the ellipsoid $\mathbf{x}^{(1)}, \mathbf{x}^{(2)}, \mathbf{x}^{(3)} \in \mathbb{R}^3$ are the eigenvectors of the matrix $\mathbf{A}$, and they are all orthogonal to each other. These eigenvectors essentially define the principal reference system of the ellipsoid. Let $\alpha$,$\beta$ and $\gamma$ be the yaw, pitch and roll angles that define the orientation of the principle reference system of the ellipsoid, with respect to the base reference system. The rotation matrix describing the ellipsoid principal reference system with respect to the base reference system is given by:

$$\mathbf{R}(\alpha, \beta, \gamma) = \mathbf{R_z}(\alpha)\mathbf{R_y}(\beta)\mathbf{R_x}(\gamma) \tag{4.15}$$

Solving (4.15) for the $\alpha$, $\beta$ and $\gamma$ orientation angles,

$$\begin{aligned} \alpha &= tan^{-1}\left(\frac{r_{21}}{r_{11}}\right) \\ \beta &= tan^{-1}\left(\frac{-r_{31}}{\sqrt{r_{32}^2 + r_{33}^2}}\right) \\ \gamma &= tan^{-1}\left(\frac{r_{32}}{r_{33}}\right) \end{aligned} \tag{4.16}$$

where $[\mathbf{x^{(1)}} \quad \mathbf{x^{(2)}} \quad \mathbf{x^{(3)}}] = \begin{bmatrix} r_{11} & r_{12} & r_{13} \\ r_{12} & r_{22} & r_{23} \\ r_{13} & r_{23} & r_{33} \end{bmatrix}$.

The equatorial radii $a$, $b$ and the polar radius $c$, along the principal axes $\mathbf{x}^{(1)}, \mathbf{x}^{(2)}$ and $\mathbf{x}^{(3)}$ respectively of the ellipsoid are given by: $a = \frac{1}{\sqrt{\lambda_1}}$, $b = \frac{1}{\sqrt{\lambda_2}}$, $c = \frac{1}{\sqrt{\lambda_3}}$ where $\lambda_1$, $\lambda_2$, $\lambda_3$ are the eigenvalues of the matrix $\mathbf{A}$.

Based on all of the above, the symmetric components of the stiffness matrices $\mathbf{K}^{(S)}$ across all configurations, were represented by ellipsoids with center at starting points $(S^{(i)}, i = 1,2,..,7)$, radii along the individual principal axes and orientation defined above. Fig.4.6 compares ellipsoids for 0% and 100% co-contraction levels for a representative subject. The figure depicts the $X-Z$ and $Y-Z$ views w.r.t the human-centered reference frame $\langle X,Y,Z \rangle$. It must be noted that the ellipsoids plotted represent the end-point stiffness at each configuration, i.e. the longer the radius in a particular direction, the higher the stiffness in that direction. The length of each of the primary, secondary, and tertiary axes of each ellipsoid averaged across the 4 subjects is also listed as $\overline{K}_1$, $\overline{K}_2$ and $\overline{K}_3$ respectively in Tables 4.5, 4.6, 4.7 and 4.8 for the various co-contraction levels.

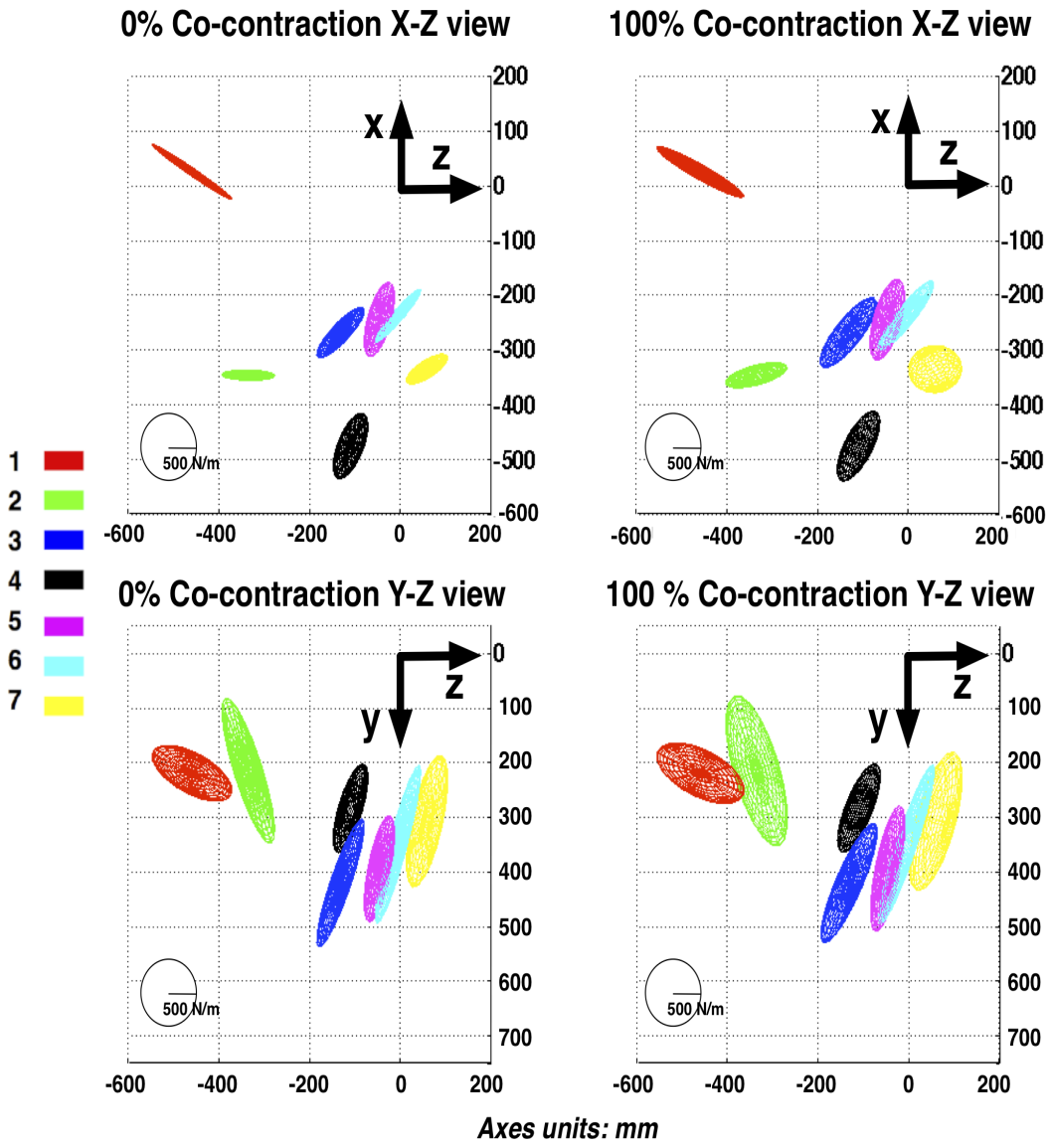


Figure 4.6: Stiffness ellipsoids for a representative subject. Check Fig. 3.1 and 3.2 for axes and configurations. The 7 different configurations are color-coded on the left.

The ellipsoids for the other three subjects for either configuration are comparatively similar in terms of the and shape and orientations. The size of the ellipsoids are also similar(with a constant scale) considering the anthropometric similarity of the subjects. This validates the impedance estimation and representation technique used. When investigated in a particular plane, the shape of the ellipses thus seen, indicate that the primary axis is aligned along the radial line joining the shoulder to the distal point of the arm. Observations

made in the shape of the ellipsoids for any configuration when increasing the co-contraction level from 0% to 100% across all the subjects show some increase in magnitude of all the axes. The maximum increase in the magnitude of the ellipsoid axes for 50%, 75% or 100% relative to the 0% co-contraction level is seen seen in the tertiary axis $K_3$. This increase is noted to be in the range of 40% to 100% for configurations 1,2,3,5 and 6 to about 250% for configurations 4 and 7. Morover, when the co-contraction level increases from 50% to 100%, the tertiary axis $K_3$ is seen to be consistently increasing in magnitude compared to the primary and secondary axes $K_1$ and $K_2$ resp. in which the magnitude more or less remains constant. These results are evident in graph plots in Fig. 4.7

Orientation changes is another observation made from the ellipsoids. A similar trend in the ellipsoid orientation is seen in the 0% co-contraction level for all the subjects. A similar trend of orientation change for increasing co-contraction levels are seen for all the subjects. The orientation changes produced in $K_1$, $K_2$ and $K_3$ by a 100% relative to 0% co-contraction level was averaged among the 4 subjects. These orientation angles changes $\Delta\theta$ are given in Table. 4.9. In terms of rotation of the ellipsoids, a 100% muscle co-contraction rotates the secondary and tertiary axes by 24.2° in average, compared to the 0% co-contraction level. Correspondingly, the ellipsoids are rotated by 8.5° on average for the primary axis indicating a change majorly in the tertiary axis.

Table 4.5: Primary, secondary and tertiary ellipsoid axes for 0% co-contraction, averaged across all subjects.

| Configuration # | $\overline{K}_1$ (N/m) | $\overline{K}_2$ (N/m) | $\overline{K}_3$ (N/m) |
|---|---|---|---|
| 1 | 2202.1 | 711.5 | 188.7 |
| 2 | 2740.1 | 661.3 | 146.6 |
| 3 | 2807.6 | 476.6 | 268.1 |
| 4 | 2046.6 | 663.4 | 471.1 |
| 5 | 2550.1 | 484.3 | 301.1 |
| 6 | 3264.9 | 505.1 | 247.7 |
| 7 | 2549.9 | 845.9 | 368.3 |

Table 4.6: Primary, secondary and tertiary ellipsoid axes for 50% co-contraction, averaged across all subjects.

| Configuration # | $\overline{K}_1$ (N/m) | $\overline{K}_2$ (N/m) | $\overline{K}_3$ (N/m) |
|---|---|---|---|
| 1 | 2421.0 | 799.6 | 282.2 |
| 2 | 2841.2 | 910.3 | 265.0 |
| 3 | 2887.5 | 541.6 | 330.2 |
| 4 | 2108.3 | 747.3 | 538.7 |
| 5 | 2725.4 | 574.0 | 356.7 |
| 6 | 3438.4 | 570.0 | 324.2 |
| 7 | 2721.6 | 955.0 | 600.4 |

Table 4.7: Primary, secondary and tertiary ellipsoid axes for 75% co-contraction, averaged across all subjects.

| Configuration # | $\overline{K}_1$ (N/m) | $\overline{K}_2$ (N/m) | $\overline{K}_3$ (N/m) |
|---|---|---|---|
| 1 | 2499.6 | 921.8 | 253.0 |
| 2 | 2928.7 | 894.3 | 318.1 |
| 3 | 2949.5 | 585.7 | 369.4 |
| 4 | 2132.0 | 755.6 | 582.6 |
| 5 | 2731.3 | 582.1 | 363.5 |
| 6 | 3518.9 | 590.9 | 361.0 |
| 7 | 2701.0 | 1022.4 | 686.9 |

Table 4.8: Primary, secondary and tertiary ellipsoid axes for 100% co-contraction, averaged across all subjects.

| Configuration # | $\overline{K}_1$ (N/m) | $\overline{K}_2$ (N/m) | $\overline{K}_3$ (N/m) |
|---|---|---|---|
| 1 | 2406.5 | 910.1 | 414.2 |
| 2 | 2924.1 | 1090.4 | 355.2 |
| 3 | 2955.3 | 579.3 | 374.0 |
| 4 | 2182.5 | 845.5 | 608.0 |
| 5 | 2827.8 | 642.2 | 393.4 |
| 6 | 3471.0 | 627.6 | 417.7 |
| 7 | 2701.0 | 1191.2 | 667.5 |

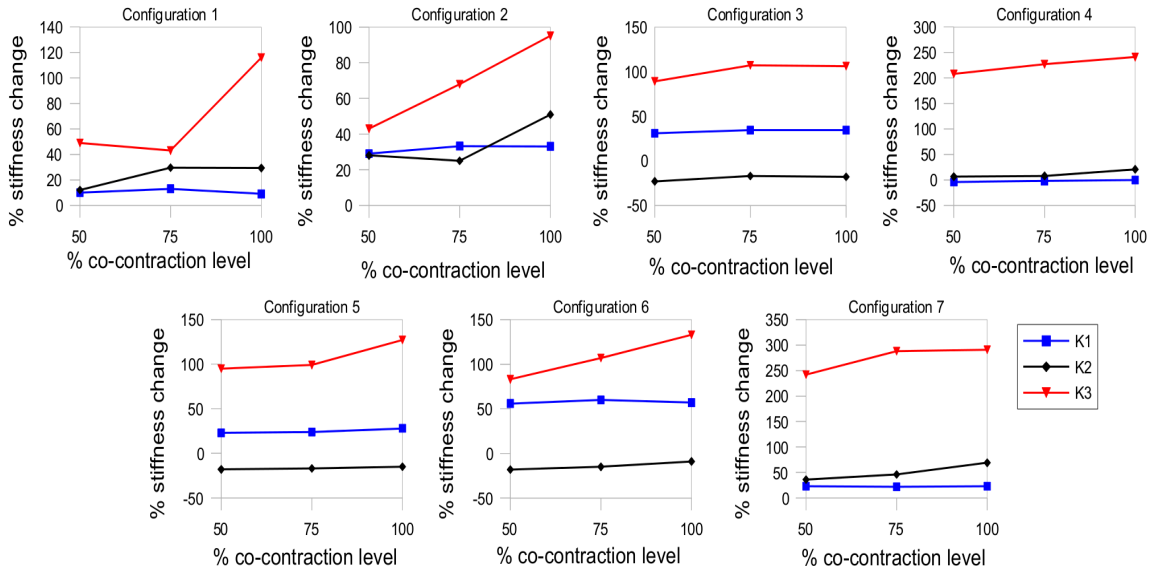


Figure 4.7: Increase of arm stiffness along the primary, secondary, and tertiary axes of the ellipsoids for the different co-contraction levels.

Table 4.9: Rotation angles of the primary, secondary, and tertiary axes of of stiffness ellipsoids from 0% to 100% co-contraction.

| Configuration # | $\Delta\theta_1(^\circ)$ | $\Delta\theta_2(^\circ)$ | $\Delta\theta_3(^\circ)$ |
|---|---|---|---|
| 1 | 26.0 | 32.2 | 27.7 |
| 2 | 6.6 | 12.4 | 14.8 |
| 3 | 5.7 | 25.8 | 27.3 |
| 4 | 6.7 | 35.2 | 35.1 |
| 5 | 4.9 | 16.5 | 16.2 |
| 6 | 3.7 | 23.6 | 23.8 |
| 7 | 6.5 | 23.7 | 24.5 |

The discussion on ellipsoid size, shape and orientation discussed above can be summarized using a 3D plot of the equatorial radii of the ellipsoid along the primary, secondary and tertiary axes. Fig. 4.8 shows a 3D plot of these radii along the primary, secondary and tertiary axes for 0% and 100% co-contraction levels of a representative subject. Firstly, it can be observed that the relation primary radius $>$ secondary radius $>$ tertiary radius is maintained as co-contraction level increases from 0% to 100%. This indicates a consistent

shape of the ellipsoids from one level to the other. Moreover, both the length of the radius along and orientation of the primary axis do not change significantly. But, the same holds true for the both secondary and tertiary axes consistently throughout all the 7 configurations indicating an anisotropic change in the size and orientation of the ellipsoids. The same observations were made for the other 3 subjects.

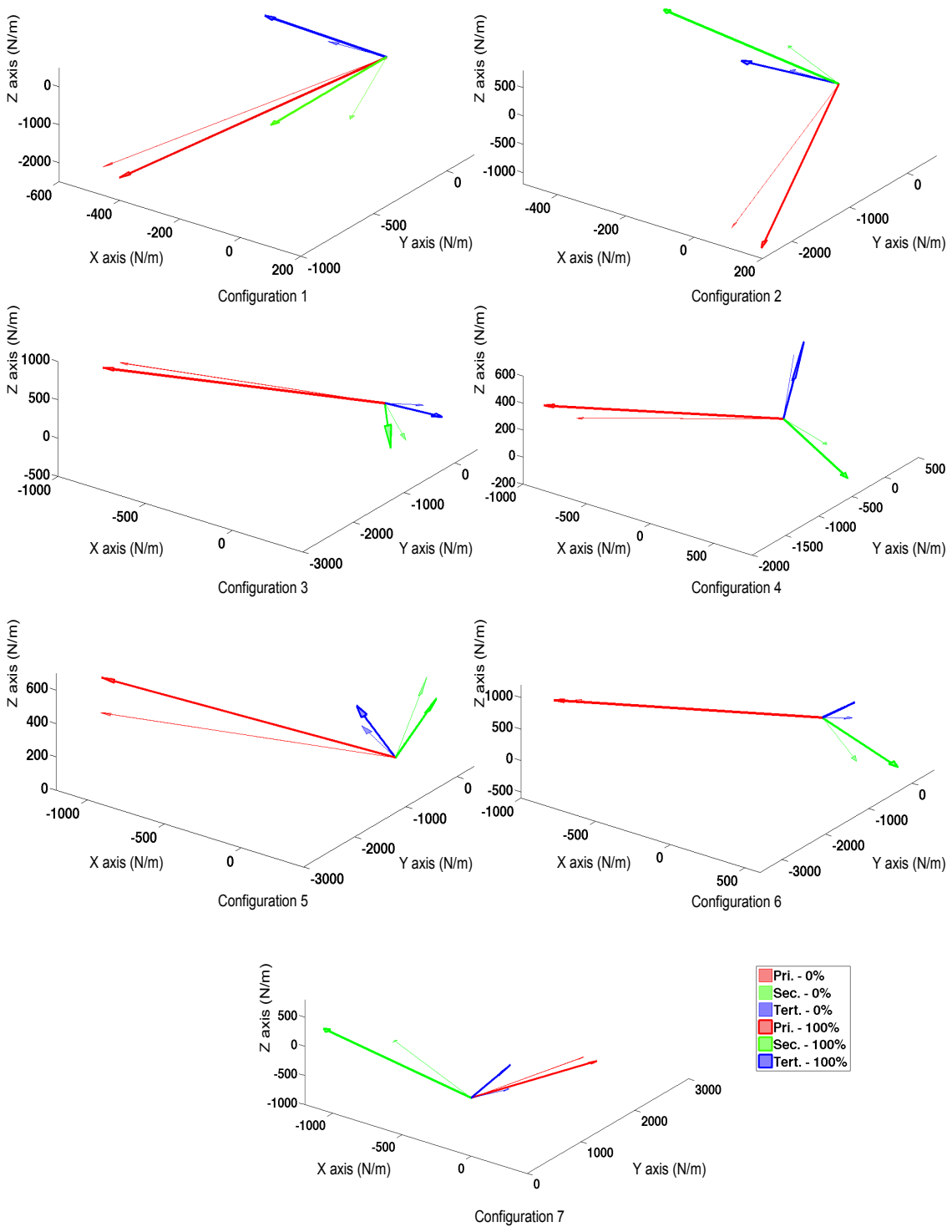


Figure 4.8: Representative 3D plots of equatorial ellipsoidal radii along primary, secondary and tertiary axes for 0% and 100% co-contraction levels of a representative subject across 7 configurations.

# Chapter 5

# DISCUSSIONS

The results obtained were consistent among the 4 subjects that participated in the study validating the method introduced for characterizing impedance in 3D in this thesis. It was observed that the restoring forces due to inertia ($I$) and damping ($B$) were very small compared to the ones due to arm stiffness, especially in the cases involving muscle co-contraction. For that reason, it is not certain that they were accurately identified using the least-squares equation. The range of stiffness values estimated are very close to those reported in the literature for the 2D case [7, 30, 31, 36]. Moreover, the antisymmetric components of the stiffness were observed to be much lower then the symmetric components, which proves that the forces produced in the arm due to the perturbations were conservative i.e. purely due to the spring like mechanism, which agrees with the literature for planar arm configurations [26]. The results show that there is a significant effect of both the arm configuration and the muscle activation level on arm stiffness. This effect is reflected on the relationship between the stiffness ellipsoids and muscle co-contraction. The hypothesis assumed before the experiments was that the stiffness will increase isotropically along all the axes of the ellipsoids. Fig.4.7 shows the percent increase of arm stiffness along the primary, secondary, and tertiary axes of the ellipsoids for the different co-contraction levels. Reported values are averaged across subjects. As it can be seen from Tables 4.5, 4.6, 4.7 and 4.8, as well as Fig.4.7, muscle co-contraction *enlarges* the stiffness ellipsoid primarily along the tertiary axis and somewhat along the secondary axes. The ellipsoids didn't significantly change along the primary axis, with a maximum overall change of 50% observed only in a few configurations. But an overall change ranging between 40% to 100% for configurations 1,2,3,5 and 6 to about 250% for configurations 4 and 7 was observed in the tertiary axis. In terms of rotation of the ellipsoids, a 100% muscle co-contraction level rotates the secondary and tertiary axes by 24.2° in average, relative to the 0% co-contraction level. Correspondingly, the ellipsoids are rotated by 8.5° on average for the primary axis.

## 5.1 Conclusion

From these observations we can conclude that muscle co-contraction induces an anisotropic change of the arm stiffness, affecting primarily the secondary and tertiary axes of the ellipsoids, and not the primary axis. The primary axis has a higher stiffness magnitude compared to the other two axes, by virtue of the arm kinematics. It can be concluded that this primary axis has a limitation in terms of how much more the stiffness can be altered by co-contracting muscles along that axis. And instead the natural mechanism underlying muscle co-contraction increases the stiffness along the needed weaker axes. A possible explanation of this phenomenon is the way individual muscles contribute to this change of the overall arm stiffness, which is a function of both the configuration of the arm, as well as the properties of each muscle independently. However, it is worth noting that the results are very consistent across subjects, which proves the validity of the proposed method, as well as the possibly groundbreaking importance in the study of the biomechanics of the human upper limb, with a plethora of implications for the EMG-based control of orthotic devices.

## 5.2 Future Research

Since muscle co-contraction essentially does not alter the inertia of the arm in any configuration, a bio-mechanical analysis can be done to identify the inertia which was poorly identified in proposed method. Although previous work in the field indicate that the damping does not change significantly due to isometric muscle co-contraction a different perturbation method or impedance estimation method e.g force regulation tasks can be performed to identify the damping.

A further investigation of the geometry of the musculoskeletal models, as well as the contribution of each muscle to the overall arm Cartesian stiffness should be conducted to give more insight to the results.

With the understanding developed from the this study, the characterization of impedance

and how it is regulated through muscle co-contraction can be transformed to a multi-joint arm movement while interacting with the environment scenario.

REFERENCES


[1] *KUKA LWR4+ Operating Instructions*. KUKA Roboter GMBH, 2011. vii, 31

[2] A. M. Acosta, R. F. Kirsch, and E. J. Perreault. A robotic manipulator for the characterization of two-dimensional dynamic stiffness using stochastic displacement perturbations. *J. Neuroscience Methods*, 102:177–186, 2000. 7

[3] E. Bizzi, N. Accornero, W. Chappel, and N. Hogan. Arm trajectory formations in monkeys. *Exp. Brain Res*, 46:139–143, 1982. 1

[4] E. Bizzi, P. Dev, P. Morasso, and A. Polit. Effect of load disturbances during centrally initiated movements. *J. Neurophysiology*, 41:542–546, 1978. 1

[5] E. Bizzi, F. A. Mussa Ivaldi, and N. Hogan. Regulation of multi-joint arm posture and movement. *Progess in Brain Research*, 64, 1986. 1, 2

[6] E. Bizzi, A. Polit, and P. Morasso. Mechanisms underlying achievement of final head position. *J. Neurophysiology*, 39:435–444, 1976. 1

[7] E. Burdet, R. Osu, D. W. Franklin, T. Yoshioka, T. E. Milner, and M. Kawato. A method for measuring endpoint stiffness during multi-joint arm movements. *Journal of Biomechanics*, 33:1705–1709, 2000. 7, 9, 25, 57

[8] Chen, Ciocarie, Cousins, Grice, Hawkins, Hsaio, Kemp, King, Lazewtsky, Leeper, Nyugen, Paepcke, Pantofaru, Smart, and Takayama. Robots for Humanity: User-Centered design for Assitive Mobile Manipulation. *IEEE Conf. on Intelligent Robots and Systems*, 2012. 3

[9] J. R. Cram and G. S. Kasman. *Introduction to Surface Electromyography*. Aspen Publishers, Inc. Gaithersburg, Maryland, 1998. viii, 36

[10] J. M. Dolan, M. B. Friedman, and M. L. Nagurka. A testbed for measurement of uman arm impedance parameters. *IEEE Conf. Syst. Eng., Pittsburg, PA*, pages 123–126, 1990. 7

[11] John M. Dolan, Mark B. Friedman, and Mark L. Nagurka. Dynamic and loaded impedance components in the maintenance of human arm posture. *IEEE Trans Systems, Man, and Cybernetics*, 23:698–709, 1993. vi, vii, 3, 7, 9, 13, 15, 16, 20, 25

[12] A. G. Feldman. Functional tuning of the nervous system with the control of movement or maintenance of steady posture III. Mechanographic analysis of the execution by man of the simplest motor tasks. *Biophysiology*, 11:766–775, 1966. 1

[13] T. Flash and F. A. Mussa-Ivaldi. Human arm stiffness characteristics during the maintenance of posture. *Exp Brain Res*, pages 315–326, 1990. 25

[14] H. Gomi and R. Osu. Task-dependent viscoelasticity of human multijoint arm and its spatial characteristics for interaction with environments. *J Neurosci*, 18:8965–8978, 1998. vii, 16, 23, 24, 35

[15] P. L. Gribble, L. I. Mullin, N. cothros, and A. Mattar. Role of co-contraction in Arm Movement Accuracy. *J. Neurophysiology*, 89:23962405, 2003. 35

[16] S. Grillner. The role of muscle stiffness in meeting hte changing postural and locomoter requirements for force development by the ankle extensors. *Acta Physiol. Scand.*, 86:92–108, 1972. 1

[17] N. Hogan. Tuning muscle stiffness can simplify control of natural movement. *Advances in Bioengineering, V. C. Mow, Ed. New York: ASME.*, pages 279–282, 1980. 1

[18] N. Hogan. Adaptive control of mechanical impedance by coactivation of antagonist muscles. *Automatic Contrl, IEEE Transactions*, 29:681–690, 1984. 2

[19] J. A. S. Kelso. Motor Control mechanisms underlying human movement reproduction. *J. Exp. Psychology*, 3:529–543, 1977. 2

[20] J. A. S. Kelso and K. G. Holt. Exploring a vibratory systems analysis of human movement production. *J. Neurophysiology*, 43:1183–1196, 1980. 1, 2

[21] D. A. Kistemaker, J. D. Wong, and P. L. Gribble. The central nervous system does not minimize energy cost in arm movements. *J. Neurophysiology*, 1994. vi, 2

[22] Peter Konrad. The ABC of EMG: A practical introduction to Kinesiological Electromyography. 2005. viii, 34

[23] H. Kusumoto, H. J. Park, and M. Akazawa. Simultaneous modulation of force generation and mechanical property of muscle in voluntary contraction. *Biomechanims (in Japanese)*, 12, 1994. 2

[24] J. M. Lanman. Movements and the mechanical properties of the intact human elbow joint. *PhD. dissertation, Dep. Psychology, MIT*, 1980. 2

[25] L. Masia, G. Sandini, and P. G. Morasso. A novel mechatronic system for measuring end point stiffness. *IEEE Conf. on Rehab. Robotics*, 2011. vi, 11

[26] F. A. Mussa-Ivaldi, N. Hogan, and E. Bizzi. Neural, mechanical, and geometric factors subserving arm posture in humans. *J Neurosci*, pages 2732–2743, 1985. v, vi, vii, 3, 6, 7, 8, 9, 12, 15, 17, 18, 19, 21, 22, 25, 41, 57

[27] Gerald O'Neill, Harshil Patel, and Panagiotis Artemiadis. An intrinsically safe mechanism for physically coupling humans with robots. *IEEE Int. Conf. on Rehabilitation Robotics*, 2013. 26

[28] R. Osu and H. Gomi. Multijoint muscle regulation mechanisms examined by measured human arm stiffness and EMG signals. *J Neurophysiol*, 81:1458–1468, 1999. 2, 25

[29] E. J. Perreault, R. F. Kirsch, and A. M. Acosta. Multiple-input, multiple-output system identification for the characterization of limb stiffness dynamics. *Biol. Cybern*, 80:327–337, 1999. 13

[30] E. J. Perreault, R. F. Kirsch, and P. E. Crago. Effects of voluntary force generation, on the elastic components of endpoint stiffness. *Exp Brain Res*, 141:312–323, 2001. 7, 10, 16, 25, 57

[31] E. J. Perreault, R. F. Kirsch, and P. E. Crago. Voluntary control of static endpoint stiffness during force regulation tasks. *J Neurophysiol*, 87:2808–2816, 2002. 25, 57

[32] M. C. Pierre and R. F. Kirsch. Measuring dynamic characteristics of the human arm in three dimensional space. *Proceedings of the Second Joint EMBS/BMES Conference*, 3:2558–2560, 2002. 3, 25

[33] R. A. Schmidt and C. McGown. Terminal accuracy of unexpectedly loaded rapid movements: Evidence for a mass-spring mechanism in programming. 2

[34] Lorenzo Sciavicco and Bruno Siciliano. *Modeling and control of robot manipulators*. McGraw-Hill, 1996. vii, viii, 27, 30, 32

[35] R. B. Stein. What muscle variable(s) does the nervous system control in limb movement. *The Behavioral and Brain Sciences*, 5:535–577, 1982. 1

[36] T. Tsuji and M. Kaneko. Estimation and modeling of human hand impedance during isometric muscle contraction. *ASME Dynamics Systems and Control Division*, 58:575–582, 1996. 7, 10, 22, 25, 57

[37] T. Tsuji and M. Kaneko. Human arm stiffness and equilibrium-point trajectory during multi-joint movement. *Biol. Cybern.*, 76:163–171, 1997. vi, 7, 8, 9, 10, 14, 23

[38] T. Tsuji, P. G. Morasso, K. Goto, and K. Ito. Human hand impedance characteristics during maintained posture. *Biol Cybern*, pages 475–485, 1995. v, vi, vii, 3, 7, 10, 11, 13, 18, 19, 20, 22, 25